Kingdom of Saudi Arabia
Ministry of Education
Qassim University
Faculty: College of Science
Department: Physics

Study of Structure and Optical Properties of TiO_2 Doped with Metals

A Thesis Submitted in Partial Fulfillment of the Requirements

for the master degree in Solid State Physics

By

Dalal Ayad ALmutairi

(431214724)

Supervisor

Dr. Aiyeshah Mohammad Alhodaib

Associate Professor in The Faculty of Science

(2025AD/1446H)


بسم الله الرحمن الرحيم

إقرار

أقر بأنني التزمت بقوانين جامعة القصيم وأنظمتها واللوائح المتعلقة بإعداد الرسائل العلمية ،وقد قمت بإعداد رسالتي وذلك بما ينسجم مع الأمانة العلمية ،والمعايير الأخلاقية كافة المتعارف عليها شخصياً دوليا في كتابة الرسائل العلمية والبحث العلمي .كما أقر بأن رسالتي هذه غير منقولة أو مستله أو منتحلة من رسائل أو كتب أو أبحاث أو أي منشورات علمية تم نشرها أو تخزينها في أي وسيلة إعلامية ،ولم يسبق تقديمها للحصول على أي درجة علمية أخرى ،وعليه أتحمل المسؤولية بأنواعها كافة فيما لو تبين غير ذلك .

الاسم: دلال عائض سالم المطيري

الرقم الجامعي: (431214724)

التوقيع:

ACKNOWLEDGMENT

First, I thank God Almighty for fulfilling my dream and completing this work. I would like to express my thanks and gratitude to my father, mother, husband, children, family and friends for their unlimited support and encouragement to me in all stages of my master's degree from study to research. I would like to express my special thanks to my supervisor, Dr. Aiyeshah Mohammad Alhodaib, for her fruitful and helpful guidance, support, and great assistance throughout the course of this research. I also thank Qassim University for giving me this wonderful opportunity.

Study of Structure and Optical Properties of TiO_2 Doped with Metals

BY

Dalal Ayad Almutairi

Recommendation of the Committee:

The Committee has approved this dissertation as a partial Completion of the requirement for a master's degree in Solid State Physics.

Examination and Decision-Making Committee

Committee members	Name	Academic Degree	Specialties action	Signature
Advisor	Dr. Aiyeshah Alhodaib	Associate Professor	Solid State Physics	
Internal Examiner	Dr. Suzan Abd El All Mahmoud	Assistant professor	Material science	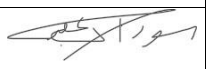
Internal Examiner	Dr. Zeinebou Yahya	Associate Professor	Fluid Mechanics and Applications	

(1446/2025AD)

Study of Structure and Optical Properties of TiO_2 Doped with Metals

BY

Dalal Ayad Almutairi

Abstract

Copper oxide (CuO)-doped titanium oxide (TiO_2) nanocomposites are promising materials for cost-effective, reliable and solar energy–saving applications while facilitating the development of alternative commercial products for solar production and energy storage, thereby increasing their efficiency in desired applications. This study investigates how different CuO concentrations affect the optical and structural properties of TiO_2, which was prepared using the sol–gel method. The analysed CuO concentrations were from 5% to 15%. The crystal structure and optical properties of the synthesised samples were analysed via X-ray diffraction, ultraviolet–visible spectroscopy and scanning electron microscopy. The samples exhibited an anatase TiO_2 crystal structure, with the crystal size increasing from 100.9 nm to 207.3 nm as the CuO concentration increased. The increased concentration affected the optical parameters by enhancing the optical proficiency of the prepared nanocomposites with a noticeable shift to the visible region to improve their efficiency in photocatalytic and energy-saving applications. This study yielded significant insights into the advancement of optoelectronic applications in industries by reducing costs, which could be instrumental in enhancing cost-effective production processes for industrial operations.

Contents

List of abbreviations

hkl	Miller indices
d	interplanar spacing
%	Percent
Nm	Nanometer
Mm	Millimeter
℃	Degrees Celsius
Cm	Centimeter
M	Meter
Se	Second
A	Angstrom
UV	Ultravioletlight
RT	Room Temperature
SEM	Scanning electron microscopy
XRD	X-Ray diffraction
FWHM	Full width at half maximum
E_g	Optical gap Energy
λ	Wavelength

List of Figures

List of Tables

Chapter 1

Chapter 1 Introduction and Literature Review

1.1 Introduction

Solar power is one of the primary renewable energy sources on Earth, which can enhance global energy security[1]. Metal–semiconductor industries are currently undergoing significant growth globally[2]. Metal–semiconductor industries are currently undergoing significant growth globally[3]. Semiconductor materials are important for solar cells; they are mainly selected based on their bandgap, optical properties, and charge carrier mobility[4]. Metal oxide semiconductors are cost effective, stable and environmentally friendly for use in photoelectric devices, which are beneficial under diverse ambient conditions[5]. An effective solar panel needs semiconductors with (i) a high bandgap for the window layer, enabling optimal light transmission and (ii) a narrow bandgap in the optically active layer to maximise light absorption[6]. The absorption of the visible-light spectrum can be increased by either growing a thick material layer or increasing the concentration of nanoparticles (NPs). However, this approach might lengthen the electron diffusion length within the NP network excessively, which might negatively impact the performance of the device[7]. Thus, determining the ideal layer thickness and material concentration of the device structure is crucial for absorbing the widest range of visible light and converting it into the maximum electrical energy .

Titanium dioxide (TiO_2) has garnered considerable interest lately because of its use in solar energy and photovoltaic systems such as waveguides, photocatalysts, hydrogen production, carbon dioxide reduction, pollutant degradation, microorganism inactivation and medicine[8]. TiO_2 can be synthesised in several forms: powders, bulk or thin films. However, TiO_2 is ideal for optical applications owing to their visible and infrared light transparency. TiO_2, a white solid inorganic metal oxide, is thermally stable, inexpensive, non-flammable, -soluble and -hazardous, occurring naturally in rocks and mineral sands[9].

Copper oxide (CuO) is a narrow-bandgap semiconductor and metal oxide that has been extensively studied with several reviews focusing on photovoltaic heterostructures arranged using low-cost techniques[10]. It is eco-friendly, exhibiting excellent frequency and is relatively simple to prepare. It exhibits a unique square planar coordination of Cu and oxygen[11]. To date, several methods have been used for synthesising CuO-doped TiO_2: sol–gel, thermal evaporation, coating, chemical vapour deposition, sputtering, anode oxidation and pulsed laser deposition, which can enhance the properties of the synthesised thin film by adjusting the operating condition parameters[12]. TiO_2 has three crystallographic forms: anatase (tetragonal), rutile (tetragonal) and brookite (orthorhombic) TiO_2. Rutile TiO_2 is the most stable form[13]. Moreover, the synthesis of the rutile TiO_2 phase is easier than that of anatase TiO_2 owing to its more advantageous thermodynamic properties and stability[14]. This study reports the preparation and fabrication of TiO_2/CuO cast films using the sol–gel method exhibiting good physical properties Furthermore , the effect of adding different CuO concentrations was studied. The alteration in the crystal morphological structure of the TiO_2/CuO nanocomposite was explored. X-ray diffraction (XRD) results reveal that changes in crystallinity were related to structural changes. Furthermore, the optical characteristics of the nanocomposite were analysed to understand the influence of CuO interactions on TiO_2 properties. Thus, this study provides valuable insights that can advance the industrial application of these composites at a reduced cost.

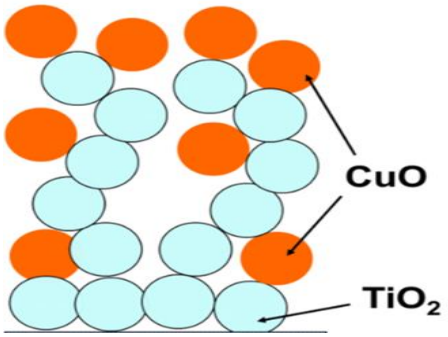

Figure (1.1) Schematic diagram of (TiO_2/CuO)[15]

1.2 Literature Review

Zaleska et al. reported TiO_2 as an excellent photocatalyst for cleansing water and air and the self-cleaning of surfaces. They reviewed various preparation methods for doping TiO_2 with metallic and non-metallic species A comprehensive examination of different dopants and the available doping techniques were reported. Visible light–activated TiO_2 was synthesised using methods such as metal-ion implantation, TiO_2 reduction and non-metal doping or sensitisation of TiO_2 using dye compounds[16].

Lee et al. have successfully synthesised TiO_2/CuO composite nanofibres with a novel structure via electrospinning, which were promising candidates for the simultaneous degradation of organic materials using photocatalysis and the generation of clean energy (hydrogen) from dye-contaminated wastewater. Furthermore, these nanofibres rapidly underwent sedimentation under gravity and exhibited remarkable sustainability[17].

Rtimi and colleagues reported the swift decline of bacterial viability in ultrathin TiO_2–Cu NP films created using high-ionisation pulsed plasma magnetron sputtering (HIPIMS). The sputtered Cu and TiO_2–Cu films completely inactivated Escherichia coli in the absence of light, a result not observed with TiO_2 alone. The presence of Cu enhanced bacterial deactivation when exposed to simulated low-intensity sunlight, highlighting its potential for practical applications. This study detailed the design, preparation, testing and surface characterisation of these developed films. Moreover, the sputtered HIPIMS composite films demonstrated significant metal savings compared to those fabricated using conventional sputtering methods[18].

Cu-doped TiO_2 was synthesised using the sol–gel method and subjected to various calcination temperatures. The as-synthesised material characterised via XRD revealed that the anatase TiO_2 phase appeared at a calcination temperature of 400°C, while it altered to the rutile TiO_2 phase at 500°C. Additionally, temperature

and doping concentration significantly influenced the crystallite phase changes in Cu-doped TiO_2[19].

Sawicka-Chudy and colleagues analysed p–n junctions formed by CuO and TiO_2 as affordable photovoltaic alternatives to silicon (Si) solar cells owing to low costs and simple production processes. This review concentrates on TiO_2–cuprous oxide (Cu2O) and TiO_2/CuO cascade heterojunctions. They highlighted the characteristics and uses of TiO_2, CuO and Cu2O. The performance indicators such as the fill factor, efficiency, open-circuit voltage, current density, layer thickness, preparation methods and electrode types of the heterojunctions comprising Cu (I) and Cu (II) oxides, and TiO_2 were emphasised. The efficiency values spanned from 0.0005% to 1.62% with TiO_2 and Cu2O layer thicknesses of 0.06–16 μm, and 0.18–1.5 μm, respectively, based on the manufacturing process. They also evaluated Cu (I) and Cu (II) oxide combinations with zinc oxide (ZnO) and Si, examining the impact of the thickness of Cu(I) and Cu(II) oxides on performance. Finally, they explored ways to enhance the efficiency in converting the energy of heterojunction solar panels with integrated CuO and TiO_2, thus advancing thin-film solar technology[20].

Raguram et al. synthesised Cu-doped TiO_2 NPs using the sol–gel method with varying Cu precursor concentrations (0.025, 0.05, 0.1 and 0.2 M). They explored the impact of Cu on the electrical, structural, compositional, morphological and optical characteristics of the NPs. TiO_2 enhanced efficiency in dye-sensitised solar cells and served as a photocatalyst. Structural analyses revealed that all samples were in the anatase TiO_2 phase with a tetragonal crystal structure, and Cu ions were effectively integrated into the TiO_2 lattice. The NPs were mostly spherical with minor agglomeration. Energy-dispersive X-ray spectroscopy (EDS) confirmed the purity of the NPs, revealing only Ti, O and Cu. Ultraviolet diffuse reflectance spectroscopy analysis shows a decrease in reflectance as Cu concentration increased, indicating that 0.1-M Cu is the ideal dopant for TiO_2 for applications in solar cells and photocatalysis[21].

Using the sol–gel technique, Yang and his group developed Cu-doped TiO_2 NPs with doping levels of 0%–2.0% and examined their crystalline structures and morphologies via XRD and X-ray photoelectron spectroscopy. They assessed their optical absorption characteristics via ultraviolet–visible (UV–Vis) absorption spectroscopy. For photocatalytic performance evaluation, they measured the degradation of methyl orange at a concentration of 20 mg L^{-1} under UV–Vis irradiation. Cu-doped TiO_2 NPs substantially improved photocatalytic activity than pure TiO_2 with optimal performance observed at a 1.0% Cu doping, attributed to enhanced light absorption and minimised recombination of electron–hole pairs[22].

Abbas and colleagues explored the synthesis of Cu-doped TiO_2 nanopowder using a traditional method to achieve different doping levels and weights. They determined the ideal conditions for creating pellets from Cu concentrations of 0%, 3%, 5% and 7% mixed with TiO_2 NPs, which were then converted into pellets and sintered at ~1100°C. Scanning electron microscopy (SEM) and XRD were used to assess the structural, morphological and mechanical characteristics of the samples. Cu doping affected the crystallinity, roughness and thermal conductivity of TiO_2 NPs. They emphasised the effect of the annealing temperature on the properties of the synthesised material[23].

Khodair et al. produced TiO_2 NPs from industrial TiO_2 and sodium hydroxide (NaOH), and CuO NPs from copper nitrate (CuNO3) and citric acid using the sol–gel method. XRD, EDS, field-emission SEM (FE-SEM) and transmission electron microscopy (TEM) results showed that TiO2 NPs exhibited an average crystallite size of 17.25 nm while CuO NPs of 15.33 nm. SEM images indicated that the crystalline forms resembled spherical nanostructures with the NPs displaying a polyhedral shape. The TEM results further validated the spherical morphology of TiO_2 and CuO NPs. Thus, this NP preparation method is highly promising[24].

1.3 Aim of the study

This thesis reports the preparation of TiO_2–CuO samples and investigates their physical characteristics (optical and structural characteristics). The samples

were prepared in a heterogeneous configuration using the sol–gel technique with different CuO concentrations. We investigated the effect of changing the concentrations on structural characteristics and lattice constants. Optical constants and changing optical characteristics were also investigated.

1.4 Thesis outlines This thesis consists of four chapters, respectively:

1.4.1 Chapter One

This chapter discusses the scientific and technological importance of studying the binary heterostructure TiO_2/CuO compound and presents earlier studies on the physical characteristics of TiO_2/CuO and their important findings.

1.4.2 Chapter Two

The second chapter examines the theoretical foundations of the structural properties of the binary heterostructure compound TiO_2/CuO. It elaborates on the methodology for calculating the optical constants of this compound, accompanied by a comprehensive delineation of the physical and mathematical models that will be employed to interpret the results.

1.4.3 Chapter Three

This chapter lists the laboratory instruments and the substrates used to prepare TiO_2/CuO nanocomposites and measure their structural and optical characteristics.

1.4.4 Chapter Four

This chapter discusses the sol–gel technique for preparing TiO_2 with different CuO concentrations. The conclusions are outlined, considering the theoretical premises discussed in the second chapter.

Chapter 2

Chapter 2 Background theory

2.1 Introduction

Materials are divided into three groups: conductors, insulators and semiconductors (Figure 2.1). Semiconductors can conduct limited electricity. Their electrical conductivity can be manipulated through the introduction of suitable dopants or by altering external factors such as temperature, pressure or electric field. Under typical conditions, semiconductors behave as insulators. However, they can conduct electricity under specific conditions, making them crucial for producing electronic components.

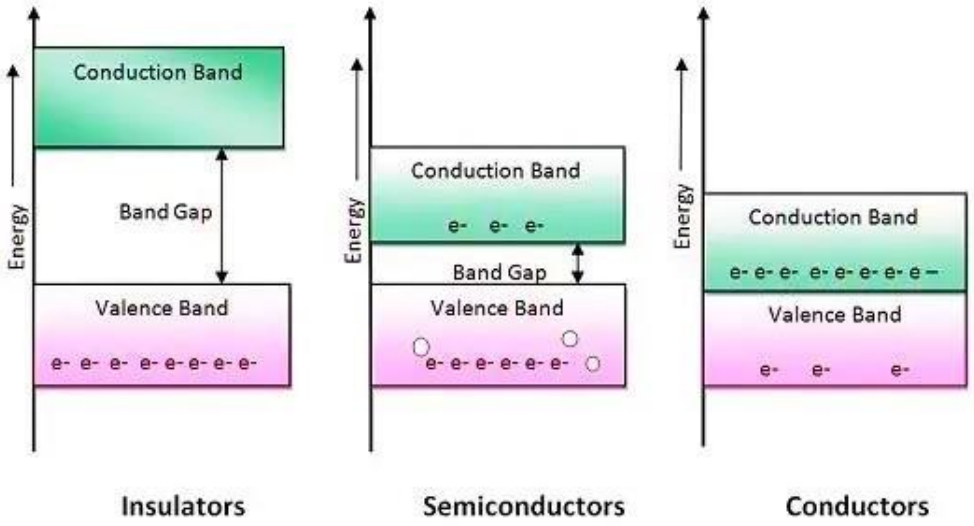

Figure (2.1) Classification of materials using energy band theory

(e^- = electrons and o = holes)[25]

Semiconductors are also used in photovoltaic technology. They can be used in solar panels for converting sunlight into electricity, as shown in Figure (2.2).

Figure (2.2) Solar panels, from applications for Semiconductors[26]

2.2 Semiconductor materials:

Semiconductors can be categorised into two main types.

1. Elemental semiconductors: They primarily include Si and germanium (Ge) .
2. Compound semiconductors: They can be further divided into inorganic [cadmium sulphide (CdS) and gallium arsenide (GaAs)] and organic semiconductors (anthracene, phthalocyanines with doping and organic polymers including polypyrrole, polyaniline and polythiophene) .

Currently, most semiconductor devices depend on elemental materials, specifically semiconductors such as Si or Ge as well as inorganic compound semiconductors[27].

2.3 Semiconductor Compounds Group IVA and IB

These compounds comprise Groups IVA and IB elements. Generally, the main aspects of the electronic structures of Groups IVA and IB elements (Figures 2.3 and 2.4) can be summarised as mentioned .

•Group IVA elements contain four paired electrons ($3d^2 4s^2$) in their outer electronic layer.

• Group IB elements exhibit a ($3d^{10} 4s^1$) configuration, which are also elements with 11 electrons in the last and penultimate orbital.

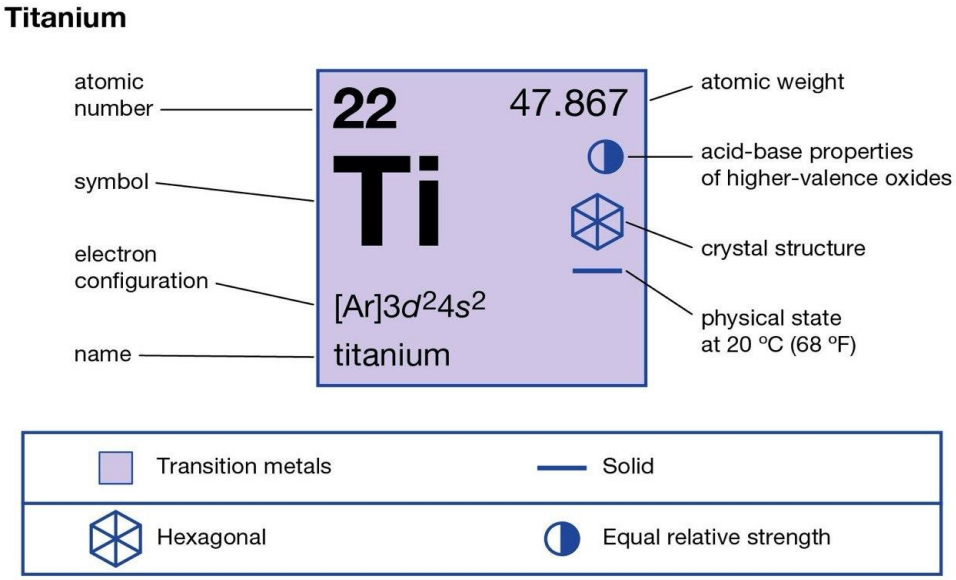

Figure (2.3) Properties of titanium (Ti)

We focussed on the semiconductor compounds produced by fusing Group IVA elements with Group IB elements (Group IVA–IB) forming a TiO_2/CuO binary complex. The heterogeneous structures of these compounds were obtained by mixing TiO_2 with different CuO concentrations, which was possible because they belong to the same group with the same electronic structure[28].

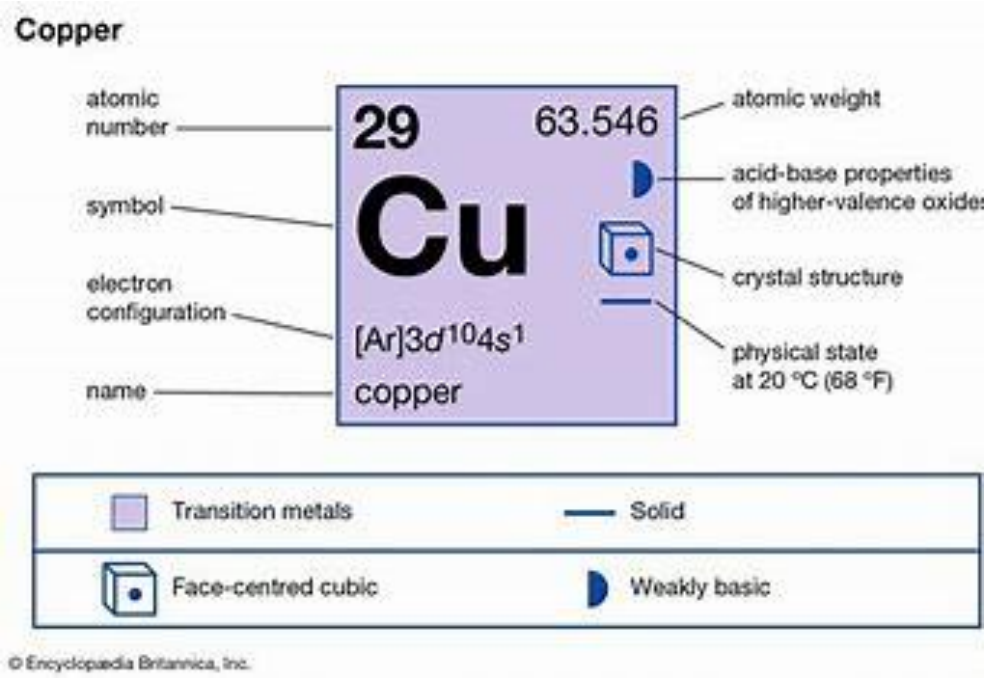

Figure (2.4) Properties of Copper (Cu)

2.4 Energy Band Gaps in Semiconductor

EC denotes the lowest energy level of the conduction band, whereas EV denotes the highest energy level of the valence band. Several closely spaced energy levels exist above EC and below EV. The energy bandgap (Eg) is the difference between the valence band peak and conduction band base with its size ranging from large to small or potentially non-existent, depending on the material. A small bandgap (Eg < 3 eV) is observed. Figure 2.5 shows that certain electrons in the valence band can gain sufficient energy to bridge the gap and move to the conduction band at room temperature. The number of electrons for conduction is finite and can move freely within the conduction band. Concurrently, electrons and holes for conduction undergo recombination, a process where electrons combine with holes.

At equilibrium, the rate of generation balances the rate of recombination, which occurs when an electron collides with a hole[29].

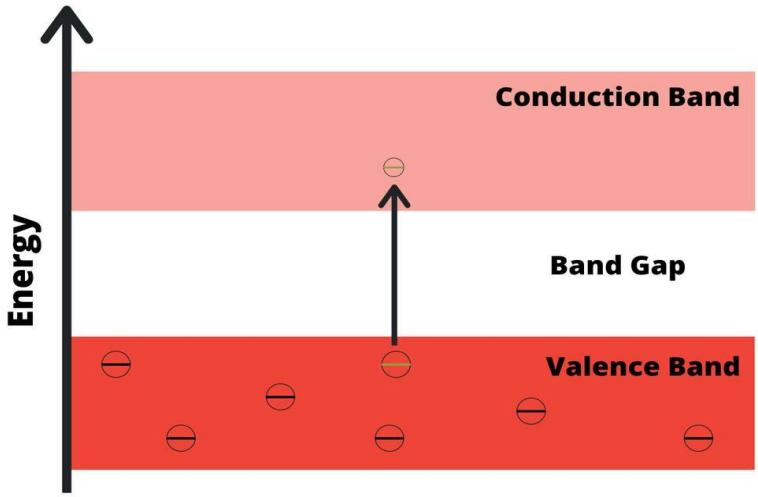

Figure (2.5) Diagram illustrating the valence and conduction bands of materials[30].

2.5 Types of Band Gaps

2.5.1 Direct Band gap Semiconductors

The force acting on a charge carrier within a crystal is expressed as Eq. (2.1).

$$F = m^* a \qquad (2.1)$$

or the product of the effective mass and acceleration. This defines the kinetic energy of a charge carrier within a crystal (Eq. 2.2).

$$E = \frac{P}{2m*} \qquad (2.2)$$

where p is the momentum of the charge carrier and m* is the effective mass. Furthermore, when an electron is excited, it absorbs a photon, creating an energy difference equal to the energy of the photon between its final and initial states. Thus, p^o and $p^{o'}$ represent the changes in crystal momentum for conduction and valence bands, respectively.

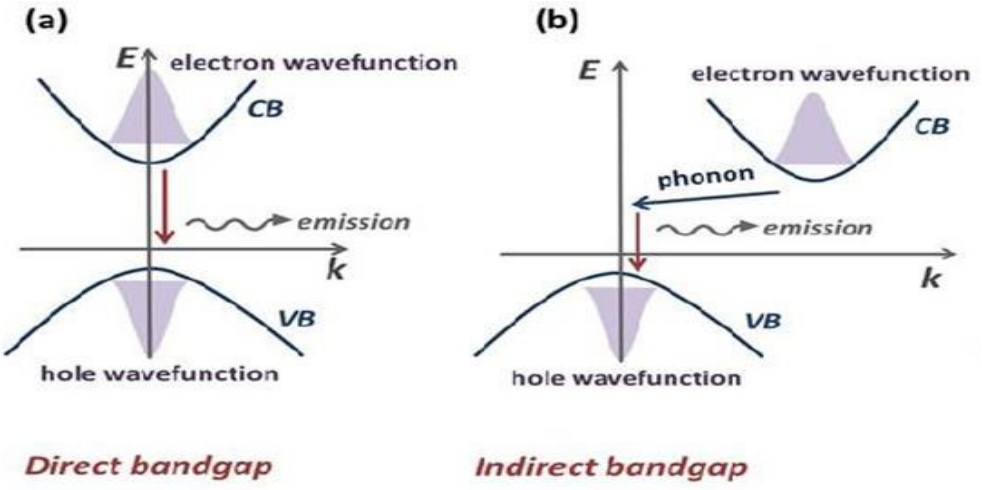

Figure (2.6) (a) Direct and (b) indirect band gap semiconductors[31].

These equations indicate that when p^o is equivalent to $p^{o'}$, the semiconductor has a direct band gap, indicating that an increase in photon energy results in a proportional increase in crystal momentum.

2.5.2 Indirect Band gap Semiconductors

If the momentum of the crystal p^o is not equivalent to $p^{o'}$, the bandgap is indirect. This indirect bandgap [Figure b(2.2)] demonstrates that the minimum energy (y-axis) of the indirect bandgap is shifted in crystal momentum (x-axis) relative to the valence curve.

2.6 Properties and Crystal Structure of TiO_2

Since the commercial production of TiO_2 in the early 20^{th} century, it has found extensive use as a pigment in a variety of products such as sunscreens and paints. Ti ranks as the fourth most abundant metal and the ninth most abundant element on Earth, constituting around 0.63% of Earth's crust. This transition metal (atomic number = 22) is lightweight, strong, lustrous and resistant to corrosion. TiO_2 is a white substance that does not dissolve in water or alcohol but dissolves in

concentrated acids. It also has no odour. As an n-type semiconductor with a wide bandgap, it can readily create electron–hole pairs under light with its three crystallographic phases: anatase, rutile and brookite with bandgaps of 3.2, 3.0 and 2.96 eV, respectively[32].

Figure (2.7) Titanium dioxide powder

Table 2. 1 crystalline characteristics of Titanium dioxide[20].

parameter	**Titanium dioxide(TiO_2)**
Molecular Weight/ Molar Mass	233.38 g/mol
Boiling Point	1,600 °C
Density	4.5 g/cm³
Melting Point	1,580 °C
Bandgap	Rutile 3.0 eV, Anatase 3.2 eV, Brookite 2.96 eV

TiO_2 is widely recognised as a strong n-type semiconductor because of its tendency for oxygen deficiency. Rutile TiO_2 features a tetragonal structure with 6 atoms per unit cell, showing lattice parameters of a = b = 4.5933 Å and c = 2.9592 Å, leading to a c/a ratio of 0.6442. Anatase TiO_2 also has a tetragonal structure, as shown in Figure (2.8). At 0 K the anatase phase exhibits more stability than the rutile phase. The anatase phase shows lattice parameters of a = b = 3.7710 Å and c = 9.430 Å, yielding a c/a ratio of 2.5134 g. Brookite TiO_2 features an orthorhombic crystal structure. It is complex with a large cell volume and is the least dense of the three forms. Furthermore, it is rarely used for experimental investigations. Brookite has

lattice parameters of a = 5.4558 Å, b = 9.1819 Å and c = 5.1429 Å with a c/a ratio of 0.6442. The Ti–Ti distances in anatase are longer (0.379 and 0.304 nm) than those in rutile (0.357 and 0.296 nm), whereas the Ti–O distances in anatase (0.1934 and 0.1980 nm) are shorter than those in rutile (0.1949 and 0.1980 nm)[33], [34].

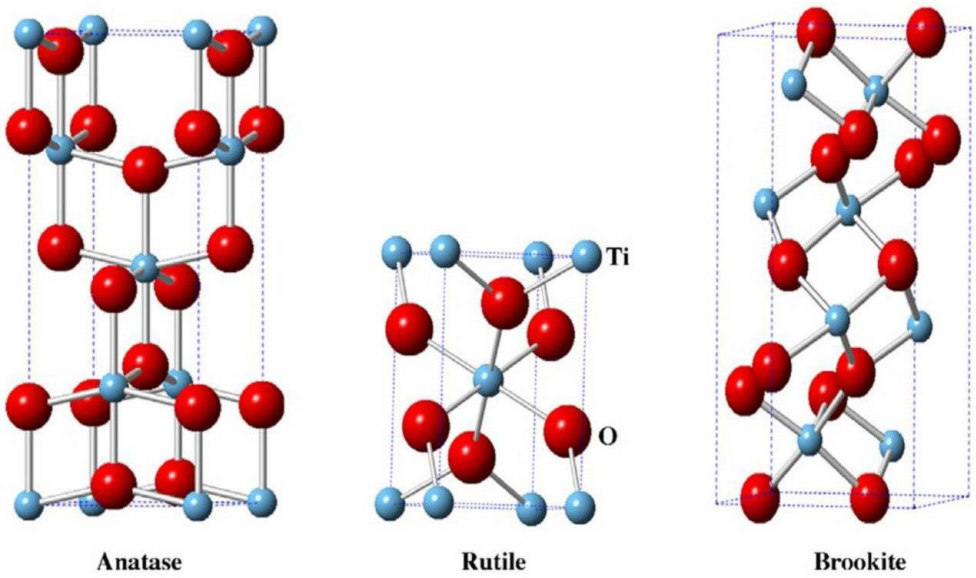

Figure (2.*8*) Unit cells of rutile, anatase, and brookite TiO_2[35].

2.7 Properties and Crystal Structure of CuO

Pure Cu is a reddish-brown metal and is recognised for its high flexibility and malleability. It has an atomic weight of 63.54, an atomic number of 29 and a density of 8.94 g cm−3. It melts at 1083°C and boils at 2595°C. At 0°C the solubility of copper sulphate (CuSO4) in water measures 143 g L−1. Cu is relatively cheap, readily combines with polar liquids such as water and polymers and shows consistent chemical and physical traits .

CuO is a p-type semiconductor with a bandgap ranging from 1.2 eV to 1.9 eV, with a monoclinic crystal structure. Referred to as cupric oxide, this black transition metal oxide is distinguished by its high thermal conductivity and various intriguing properties. CuO is the simplest copper compound, exhibiting several beneficial physical properties such as high-temperature superconductivity,

photovoltaic capabilities, high stability and antimicrobial properties. Given these advantageous properties, CuO has been extensively studied for a range of potential uses in electrochemical cells, gas sensors and magnetic storage. Additionally, CuO can exist in highly ionic nanoparticulate forms, which expands its functionality for further usability[36], [37], [38].

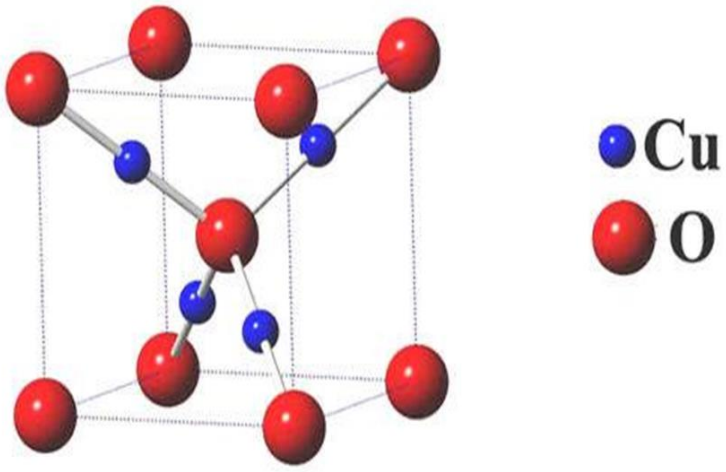

Figure (2.9) Crystal structure of CuO

Table 2. 2 crystalline characteristics of CuO[20].

Parameter	Value
Bandgap	1.2 - 1.9 ev
Density	6.515 g/cm3

2.8 Properties and Crystal Structure of the TiO_2/CuO Nanocomposite

The synthesis of TiO_2-doped Cu nanomaterials using the sol–gel method produces a compound with high physical properties.

2.9 Preparation Methods and Characterisation

2.9.1 Introduction

This chapter investigates the effect of varying concentrations of TiO_2 specifically pure TiO_2 and TiO_2/CuO with 5 wt.%, 10 wt.%, and 15 wt.% on the structural, surface, morphological and optical characteristics synthesised using the sol–gel process method. It describes the method and SEM, Fourier transform infrared spectrometry (FTIR) and XRD results for structural analysis and insights into the optical properties.

2.9.2 Sol-Gel Technique

The sol–gel technique is a commonly used chemical technique, especially a damp method, to synthesise various nanostructures, especially metal oxide NPs. A molecular precursor is dissolved, usually a metal alkoxide, in water or alcohol, heated and stirred to convert it into a gel via hydrolysis and alcoholysis. Because of the moisture content of the gel, it is dried using methods tailored to its specific properties and applications. The sol–gel technique is economical and allows to precisely control the chemical composition of the product because of its low reaction temperature. It is recognised and commonly used in industries for synthesising NPs with various chemical compositions. It focuses on forming a uniform sol from the precursors and transforming it into a gel. The solvent within the gel is subsequently removed from its structure. The drying method used has a considerable impact on its properties. Essentially, the choice of a solvent removal technique is influenced by the intended application of the gel[39].

.

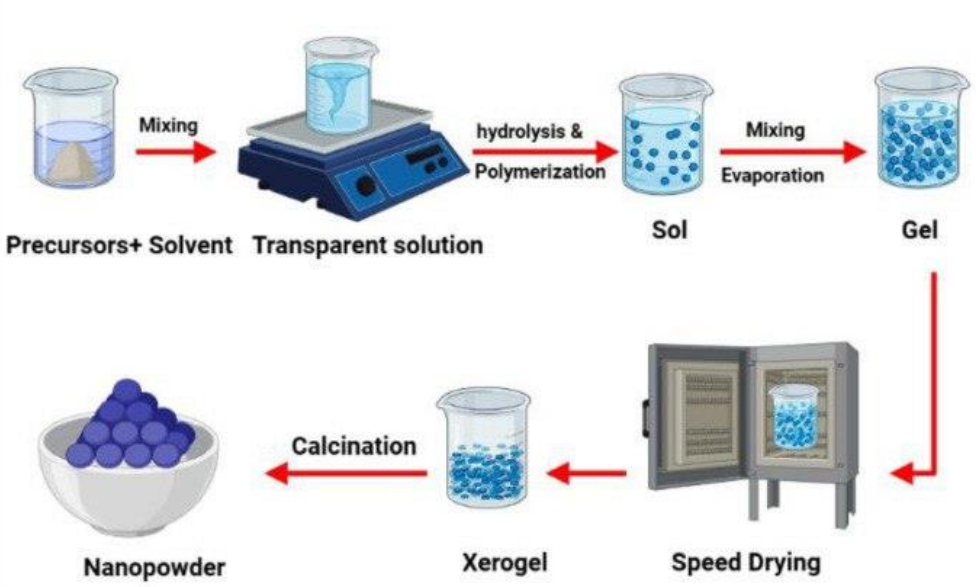

Figure (2.10) Diagram illustrating the sol-gel technique[39].

2.9.3 Scanning Electron Microscope (SEM)

SEM is the most commonly used tool for characterising and analysing the surfaces of solid samples used in research fields and industries. Scientists specialising in materials can explore the nanoscale characteristics of their samples, leading to a better understanding of the material formation and properties. It is used for examining biological samples, enabling the study of bacteria, fungi and viruses. A modern SEM includes an electron optical system, vacuum system, electronic system and computer equipped with specialised software. The electron optical system creates the electron probe and comprises several components: an electron gun, demagnification system (condenser lens), scanning unit and focusing system (objective lens, as illustrated in Figure 2.11). This system generates a highly concentrated electron probe (~1 nm in size), which scans the surface of the specimen in a raster pattern. When the electron beam interacts in the presence of the specimen, it generates various signals that detectors collect in the SEM, enabling the generation of images or spectra. It shows the generated images live on a PC monitor throughout

the scanning process. The horizontal field of view (HFW) is the scanned area. Magnification (M can be calculated using the formula M = L/HFW, where L is the width of the monitor. By keeping L constant, higher magnification is obtained by decreasing the HFW[40].

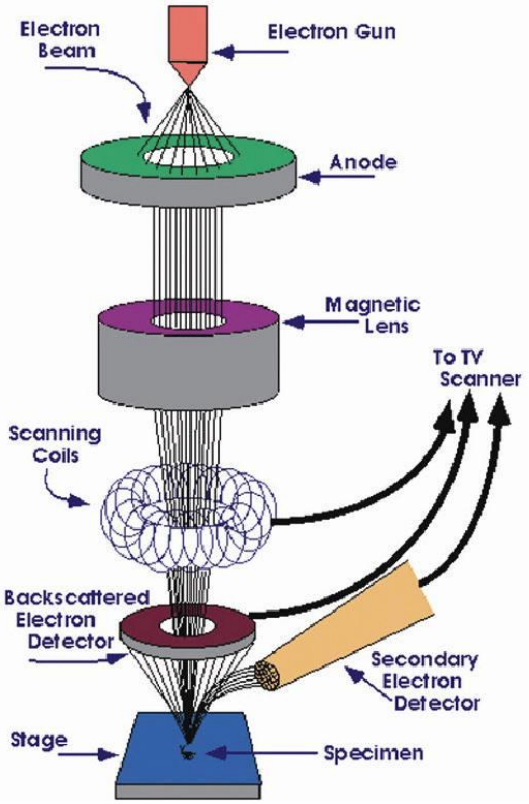

Figure (2.11) Schematic drawing of Scanning Electron Microscope (SEM)[41].

2.9.4 X-Ray Diffraction (XRD)

The XRD by crystals results from specific phase relation between two or more waves. These relations arise from variations in the path length and amplitude changes linked to phase differences. Two waves are perfectly synchronised when the difference in their path lengths is either zero or a whole multiple of the wavelength. Phase difference (A) is the difference in the path length between any two waves. When A is a whole number, which times the wavelength, the two waves synchronise flawlessly, creating a single synthesised wave with twice the amplitude of the original. The orientation of the X-ray to the crystal influences the path difference.

When A equals λ/2, the two waves cancel one another because their magnitudes are equal, but their amplitudes vary in opposition as they progress, rendering them completely out of sync. Various situations arise between these two extremes because of differing paths. The primary method for this analysis is by using Bragg's law, which incorporates the Bragg angle (Figure 3.4). The angle between the incoming X-ray beam and the plane's normal matches that formed between the normal and diffracted X-ray beam.

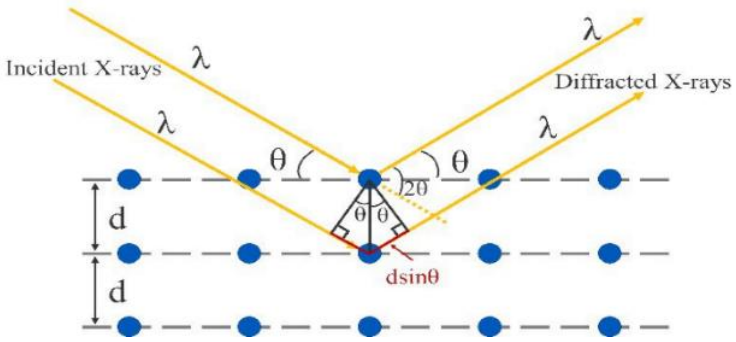

Figure (2.12): Diagram showing the X-ray diffraction by a crystal[42].

Atoms in a crystal are organised in a regular, periodic pattern. When X-ray radiation of wavelength λ strikes the crystal with an interplanar spacing d. A diffraction beam of adequate intensity becomes visible only when Bragg's law is fulfilled [Eq. (2.3)].

$$n\lambda = 2dsin\theta \qquad (2.3)$$

n represents the sequence of reflection. This pertains to the number of wavelengths in the path difference of XRD from neighbouring crystal planes (Figure 2.12). When d and d′ are defined values, diffraction occurs at different angles of incidence, such as 01, 02 and 03, which align with n = 1, 2, 3 and so forth. In first-order reflection (n = 1), the difference in path length between the two scattered X-rays denoted as 1′ and 2′ corresponds to one wavelength.

We must identify the relationship between the varying path lengths of X-rays scattered from crystals and that of the incoming X-rays. The diffraction angle 2θ

for a given set of planes (hkl) can be calculated using the plane-spacing equations. For example, in a tetragonal crystal with lattice parameter a, the interplanar spacing d and the Miller indices (hkl) are as expressed in Eq. (2.4).

$$\frac{1}{d^2} = \frac{h^2+k^2}{a^2} + \frac{l^2}{c^2} \qquad (2.4)$$

XRD is crucial for determining grain sizes and crystallinity and estimating the crystal structure using the Scherrer equation [Eq. (2.5)].

$$D = \frac{K\lambda}{\beta \cos\theta} \quad (2.5)$$

where β is the full width at half-maximum of the diffraction peak, K is a dimensionless constant, 2θ signifies the diffraction angle and λ denotes the wavelength. The assessment of crystallite size is performed by examining the broadening of a designated peak in the diffraction pattern. An increase in the concentration of the Ti dopant leads to a corresponding increase in the particle size[43].

2.9.5 UV–Vis Spectroscopy

UV and visible light constitute a minor segment of the electromagnetic spectrum, which encompasses other types of radiation, including IR and X-rays.

When materials or molecules are persistently exposed to UV–Vis–NIR (near infrared) radiation, they can absorb energy when it matches the natural modes (such as vibration and rotation) of their molecular bonds or solid structures. This leads to the formation of an absorption peak. This absorption can serve several purposes: identifying known components, investigating the formation of new chemical bonds and conducting quantitative component analysis. Optical transmittance(T) is the ratio of transmitted intensity (I_0) to incoming intensity (I). Percent transmittance is

commonly used, and absorbance(A) is also frequently utilised and defined using Eq. (2.6).

$$A = \log\left(\frac{I_0}{I}\right) = \log\left(\frac{1}{T}\right) \qquad (2.6)$$

The Beer–Lambert law indicates that absorbance (A) is directly proportional to the path length (L) and the concentration (c) of the substance absorbed [Eq. (2.7)]

$$A = \varepsilon.L.\ c \qquad (2.7)$$

where ε is the molar extinction coefficient (mol^{-1} cm^{-1}), assuming negligible reflection. A UV–Vis–NIR spectrum interprets the spectral features based on the characteristics of the sample of interest, using quantum mechanical models to connect specific atomic or molecular structures with spectral frequencies, linewidths and intensities.

2.9.6 Fourier Transform Infrared Spectrometer (FTIR)

An IR spectrum illustrates the intensity of IR light with light properties. The x-axis shows high wavenumbers on the left and low wavenumbers on the right. The spectrum displays absorbance units, which indicate the amount of light the sample absorbs. Peaks rise with their tallest points representing the wavenumbers where significant light absorption occurs. The absorbance spectrum is derived using Eq (2.6).

As Beer's law describes, absorption relates to molecule concentration in a sample[Eq. (2.7)]. In an absorbance spectrum, the height or area of a peak indicates concentration, allowing Beer's law to determine molecular concentrations in samples. Moreover, the y-axis of an IR spectrum represents percent transmittance (%T), indicating the portion of light passing through a sample[44].

2.10 The Impact of Concentration on Optical Properties

The properties of CuO can be adjusted using the preparation method, which can influence the optical bandgap and the size of crystallites. As the concentration of the structure increases, the bandgap energy decreases from 3.2 eV to 2.95 eV, while the crystal size increases with the increase in the CuO concentration from 100.9 nm to 207.3 nm[20].

2.10.1 Transmission

Absorbance indicates the amount of light absorbed. Transmittance refers to the light transmitted via a sample and is usually expressed as either a fraction or a percentage, defined as Eq. (2.8).

$$A = \log\left(\frac{I_0}{I}\right) \text{ or } \%T = \frac{I_0}{I} \times 100 \qquad (2.8)$$

In most applications, absorbance values are utilised because the connection between absorbance, concentration and path length is typically linear, according to the Beer–Lambert law [Eq. (2.9)].

$$A = \varepsilon l c \qquad (2.9)$$

where A is the absorbance, ε is the absorptivity, l is the path length and c is the concentration [44].

2.10.2 Reflection

A shiny surface such as a mirror reflects nearly all light that falls on it[45].

Chapter 3

Chapter 3 : Experimental details

3.1 Introduction

There are several chemical and physical preparation methods such as chemical vapour deposition, sol–gel, thermal evaporation, coating, sputtering, anode oxidation and pulsed laser deposition. In this chapter, we outline the methods performed to investigate the effect of CuO concentration on TiO_2. We have four samples: pure TiO_2, TiO_2/CuO (5 wt.%), TiO_2/CuO (10 wt.%) and TiO_2/CuO (15 wt.%). Moreover, we examined the structural, exterior morphology and optical properties of TiO_2/CuO samples synthesised via the sol–gel method. A detailed description of the synthesis process and characterisation (SEM, IR, XRD and optical property) results is presented.

3.2 Materials

Copper (II) chloride. titanium (IV) chloride, NaOH, ethanol and hexadecyltrimethylammonium bromide were obtained from Sigma Aldrich. All chemical reagents used were of analytical grade and used directly without further purification. Double-distilled water was used for all experiments.

3.3 Preparation of Pure TiO_2 and CuO

First, pure TiO_2 and CuO were prepared. CuO was combined with TiO_2 to synthesise the final nanocomposite. Typically, 7.5 mL of titanium (IV) chloride, the precursor, was dissolved in 25 mL of toluene. In a separate container, 1.5 g of NaOH was dissolved in 80 mL of distilled water. The NaOH solution was added incrementally to the titanium(IV) chloride solution under continuous stirring for 30 min to ensure uniformity. The pale yellow gel formed during the response was then dried at 100°C for 24 h, yielding a yellow block crystal. The synthesised materials were calcined in air at 450°C for 2 h, yielding white TiO_2. For the synthesis of pristine CuO, 2 g of copper(II) chloride was used as the precursor, which was

dissolved in 25 mL of distilled water. In a separate container, 1.5 g of NaOH was dissolved in 80 mL of distilled water. The NaOH solution was added dropwise to the copper(II) chloride solution. The mixture was stirred continuously for 30 min to achieve uniformity. During the reaction, the colour changed from dark blue to black. The gel was separated through filter paper and was subsequently rinsed with water. The sample was dried at 100°C for 1 d and then annealed at 450°C for 2 h, resulting in a black CuO residue.

3.4 Preparation of TiO_2/CuO (5wt%, 10wt% and 15wt%)

The synthesis of TiO_2/CuO nanocomposites was performed by incorporating CuO into TiO_2, following a procedure similar to that used for pure TiO_2 and CuO. Typically, after calcination, various concentrations of copper(II) chloride (0.05, 0.10 and 0.15 wt.%) and a defined volume of titanium chloride (7.5 mL) were combined. The composite films were heated on a hot plate at 35°C for 3 h to remove any left-over solvents. Finally, the composite was shaped into circular discs with dimensions of 6 mm in diameter and 0.5 mm thick for characterisation and testing.

3.5 Structure Characterisations of TiO_2/CuO Composites

3.5.1 Scanning Electron Microscopy (SEM)

SEM was used to assess and study the surface features of solid material samples. The electron optical system comprises various components: the electron probe formation apparatus that contains the electron gun, demagnification system, scanning unit and focusing system. This configuration produces a sharply concentrated electron probe that methodically scans a specific area of the specimen surface in a raster pattern. The electron beam engages with the specimen, generating various signals that specialised SEM detectors can capture, allowing real-time viewing of images or spectra on a computer display screen during SEM scanning [40].

Figure (3.1) SEM JEOL model .

3.5.2 Structural Analysis via XRD

A diffractometer is a precise device showcasing two independent axes in rotation: w and 2θ. This device collects intensity measurement data from a diffracted X-ray beam as a function of the angle, in accordance with Bragg's law and using X-rays of a specific wavelength. The basic design of the diffractometer is presented, which includes three parts: the X-ray source (F), sample holder (S) and detector (G) positioned around the circumference of a circle called the focusing circle. Once the X-ray source is secured and the detector is aligned along the 2θ axis, a flat, plate-shaped powdered sample is positioned at the centre of the diffractometer along the c-axis. This arrangement ensures that the normal vector to the sample plane aligns with the vector of scattering q, defined as the difference between the incident X-ray beam vector s_0 and the diffracted beam vectors s. Additionally, the circle that goes through points F (the focal point of the target), S (the centre of the diffractometer) and G (the focal point of the diffracted beam) is known as either the focusing circle or Rowland circle.

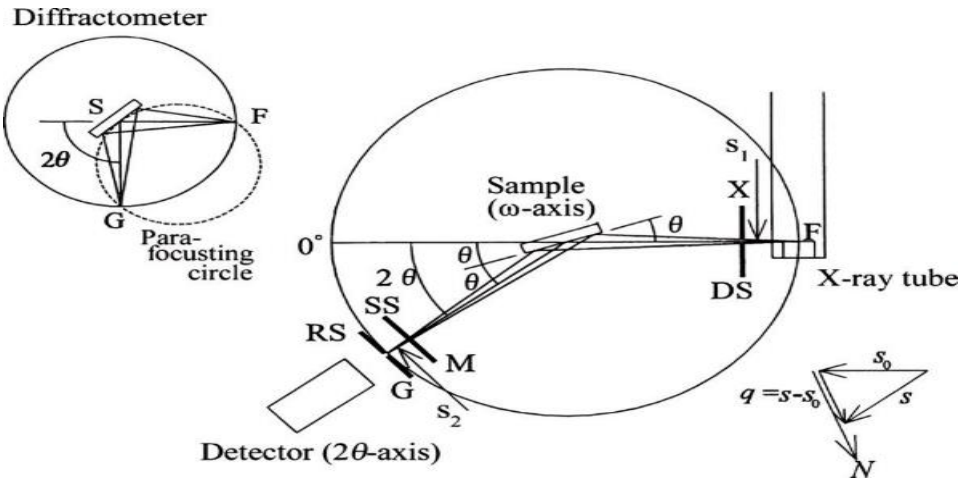

Figure (3.2) Focusing on the geometry and key aspects of an X-ray diffractometer[42]

To reduce angular dispersion and enhance the spatial resolution of the incident and diffracted X-ray beams, various slit systems are strategically placed along the X-ray pathway. A Soller slit, comprising narrowly spaced, slender metal sheets aligned with the plane of the diffractometer circle, limits the perpendicular spread of these beams. Divergent slits (DSs) and scattering slits (SSs) are designed to control the horizontal spread of incident and diffracted X-ray beams. The receiving slit (RS), positioned before the detector, is crucial for establishing spatial resolution. A notable aspect of a diffractometer is the combined dispersion limitation from DS and SS, alongside its ability to focus the diffracted X-ray beam obtained from powder samples through the RS. This method of collecting and refining data is known as para-focusing. The RS consistently matches the para-focusing point in the diffractometer, which boosts intensity measurements and improves spatial resolution[38].

Figure (3.3) X-ray diffractometer Shimadzu 6000 X-ray[46].

3.6 (UV–VIS) spectrophotometry

UV–Vis absorption spectroscopy uses a filter photometer that features either an absorption or interference filter to isolate a specific range of radiation This filter is deliberately placed between the radiation source and the sample, shielding the sample from possible harm caused by high-energy radiation exposure. A filter photometer uses a single optical path connecting the source and the detector, making it a single-beam instrument.

• Molecular UV–Vis Absorption Instrument Design

The main instrument used for molecular UV–Vis absorption is the filter photometer. It functions by isolating the bands of radiation with the specified filters, arranged to shield the sample from high-energy radiation that could lead to decomposition. In this configuration, the device is set to 0% transmittance and uses a shutter to block radiation from reaching the detector until it is activated.

• Single-Beam Spectrophotometer

A spectrophotometer is a device that uses a monochromator to select wavelengths. The fundamental model of this device is the single-beam spectrophotometer, which utilises a monochromator with a fixed wavelength. Nevertheless, single-beam spectrophotometers might pose challenges in capturing spectra because they require manual adjustments of the wavelength and recalibration, rendering the process awkward and lengthy. The precision of this type of spectrophotometer relies significantly on the consistency of its light source and detector as time progresses.

• Double-Beam Spectrophotometer

To overcome the drawbacks of fixed-wavelength single-beam spectrophotometers, the double-beam spectrophotometer is used. This device features a chopper that shifts the radiation path between the sample, blank and shutter. The signal processor relies on the established rotational speed of the chopper to distinguish between the detected signals, enabling the distinction of transmission signals for the blank (Po) and sample (Pr). This design enables constant modifications of the 0% transmittance by employing an opaque material shutter. The bandwidth of a double-beam spectrophotometer can be refined by modifying the entrance and exit slits of its monochromator, usually between 0.2 and 3.0 nm.

• Diode-Array Spectrometer

Traditional instruments using a single detector can only monitor one wavelength at once. By substituting the traditional photomultiplier with several photodiodes, we can utilise a detector array to capture a complete spectrum in 0.1 s. In a diode-array spectrometer, radiation from the source travels through the sample before being dispersed by a grating.

• Sample Cells

The sample compartment is engineered to establish a sealed setting that minimises stray radiation intrusion. Samples are usually stored in a liquid or solution form and contained within cells made of UV–Vis transparent materials such as quartz, glass

or plastic. For wavelengths under 300 nm, it is crucial to use a quartz or fused-silica cell[47].

Figure (3.4) JASCO V670 double beam spectrophotometer[48].

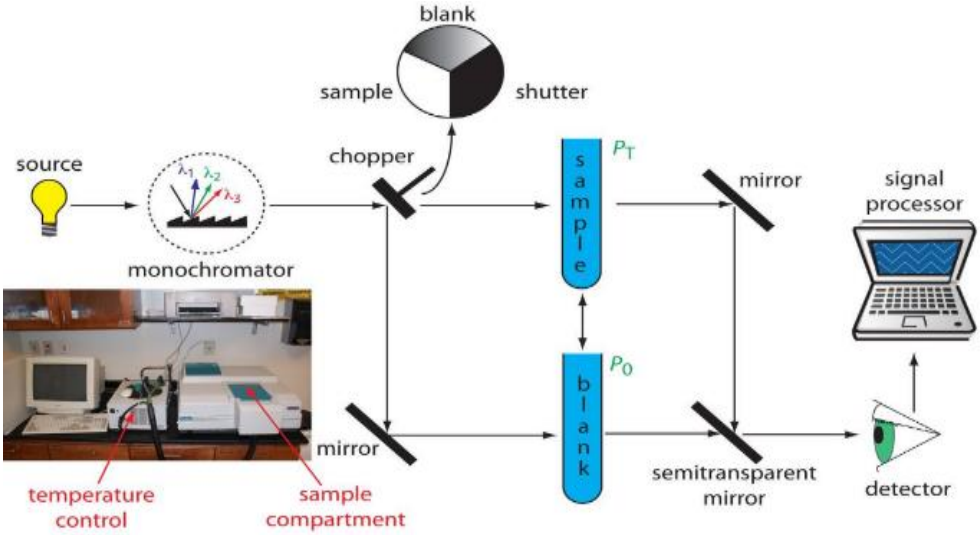

Figure (3.5) Diagram showing the UV–Vis spectrophotometer[48].

3.7 Fourier Transform Spectrometer (FT-IR):

IR microscopes capture IR spectra from tiny samples and are usually modified visible-light microscopes designed to work with the mid-IR range. The IR microscope is often situated beside the FTIR instrument, or it can be positioned directly within the sample compartment of the FTIR instrument. Microscopes typically use a light bulb to emit visible light, whereas FTIR spectrometers use IR light. Both types of light can enter through the bottom of the microscope, as shown in the illustration. A portable input mirror decides whether to illuminate the sample with IR or visible light. In some designs, the light beam passes through a lower aperture, which shapes and sizes it before reaching the sample. The next optical element it meets is the condenser, which focuses light onto the sample. A few IR microscopes utilise a Cassegrain mirror system, comprising a small convex mirror positioned above a large concave mirror, which faces upwards in this arrangement. An opening in the concave mirror allows IR light to enter and bounce off the convex surface mirror. The concave mirror focuses light onto the sample, which is mounted on a translation stage, allowing for vertical and horizontal adjustments for better focus and inspection. In Figure 3.5, the sample is shown in a transmission mode, where light travels through the sample before being directed onto the detector[39].

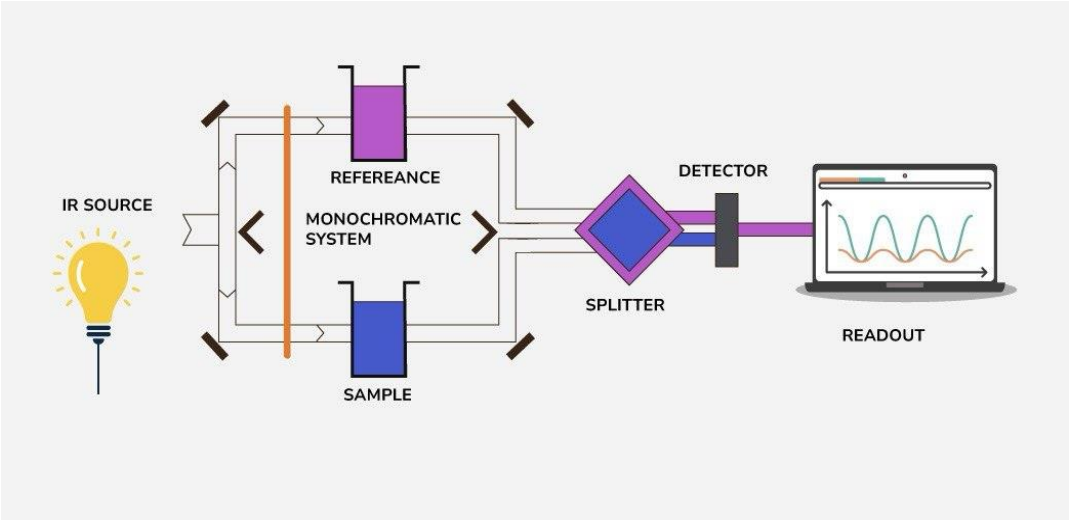

Figure (3.6) schematic of IR spectroscopy[49]

Chapter 4

Chapter 4 : Results and Discussion

4.1 Introduction

The TiO_2 samples were prepared with different concentrations of CuO using the sol-gel technique. as illustrated in Table 4.1. In the samples produced, we examined the impact of varying CuO concentrations on the structural characteristics as determined by X-ray diffraction (XRD), Fourier-transform infrared spectroscopy (FT-IR), scanning electron microscopy (SEM), and optical ultraviolet-visible (UV-Vis) properties.

Table 4. 1 the Concentration of TiO_2/CuO structure.

Sample no.	Concentration of TiO_2/CuO
a	Pure TiO_2
b	TiO_2/CuO (5 wt.%)
c	TiO_2/CuO (10 wt.%)
d	TiO_2/CuO (15 wt.%)

4.2 Structure Analysis

Instrumental effects and physical factors such as crystallite size and microstrains expand XRD peaks. Thus, the initial step is to assess the size of crystallites and lattice strain from the XRD pattern. In this study, instrumental broadening is adjusted by comparing the experimental results with those from the parabolic approximation correction [Eq. (4.1)].

$$\beta 2 = (1 - \frac{b^2}{B^2}) \qquad (4.1)$$

B and b represent the breadths (in radians) of the same Bragg peak obtained via XRD analyses of experimental and reference powders. Figures 4.1–4.5 illustrate the characteristic XRD patterns of TiO_2 and TiO_2/CuO nanocomposite photocatalysts with varying CuO ratios (5 wt.%, 10 wt.% and 15 wt.%). Each sample exhibits a clear, sharp and narrow peak, signifying the development of a highly crystalline material.

Pure TiO_2 and (TiO_2/CuO) nanocomposites are tabulated in Table 4.1. Figure 4.1 shows the diffraction lines of pure and anatase TiO_2 phases: (101), (004), (200), (211), (220), (204) and (220) at 2θ values 25.1°, 40.0°, 49.0°, 54.996°, 57.006°, 62.31° and 72°, which corresponds with the index data of JCPDS 00-001-0562. The anatase TiO_2 phase is the metastable form of TiO_2 and typically develops at low temperatures. Rutile TiO_2 (JCPDS 21-1276) is found at 2θ values of 27.72° and 38.2°, corresponding to the crystal planes (110) and (004), respectively. The highest intensity (950.5576 a.u.) is at 62.32°. Pure TiO_2 comprises anatase and rutile TiO_2, while brookite TiO_2 is absent.

The XRD pattern of TiO_2/CuO composites indicates that the ratios of CuO affect the intensity of the composites. The peak intensity of CuO increases as the amount of CuO increases. A comparison of TiO_2/CuO with a ratio of 95:5 with that of pure TiO_2 reveals that the peaks of anatase TiO_2 at 55° and 72° disappear with a slight decrease in the intensity of anatase at 25.1°.

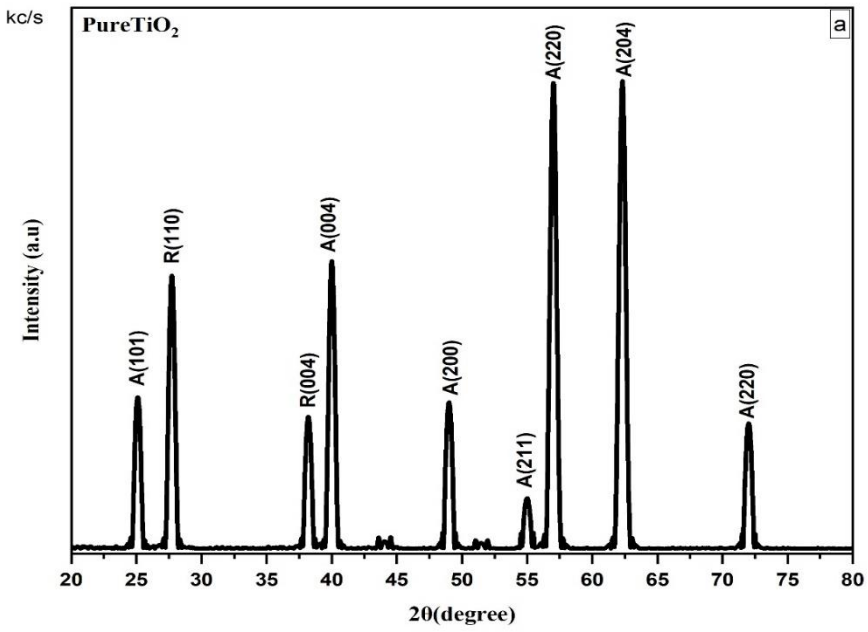

Figure (4.1) Diffraction spectra of x-rays of pure TiO_2.

Two low-intensity peaks corresponding to monoclinic CuO occur at 2θ values of 32.42° and 34.36°, associated with the (110) and (002) planes, respectively. The peak of rutile TiO_2 shifts from 38.2° to 38.48° owing to the interaction and fusion between TiO_2 and CuO. Thus, TiO_2/CuO (95:5) indicates that the incorporation of CuO with 0.5 wt.% does not alter the crystal structure of the sample. No distinctive peaks associated with CuO are detected owing to the minimal quantity of CuO present in this sample.

We were unable to distinctly identify the XRD peaks of the monoclinic phase of CuO because the lattice constants of tetragonal anatase TiO_2 closely resemble those of CuO.

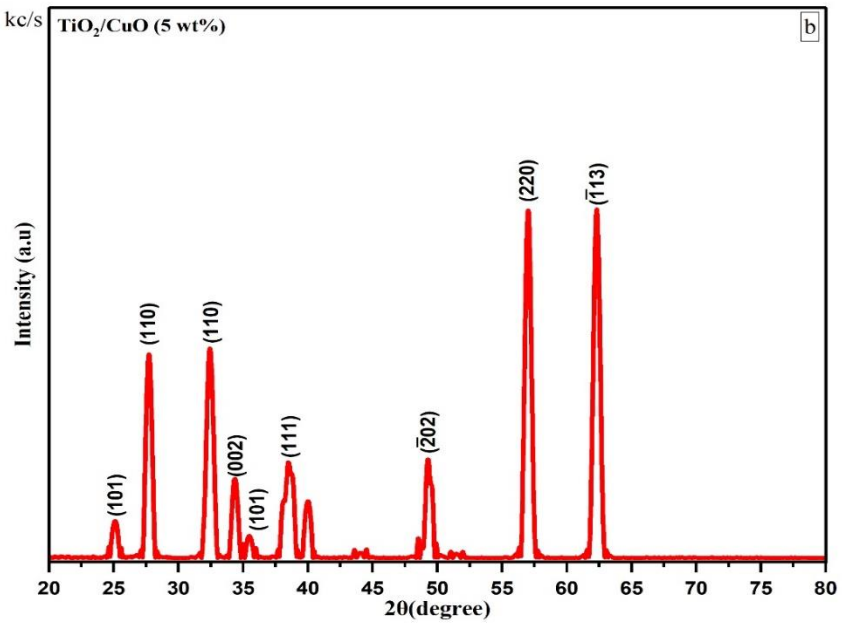

Figure (4.2) Diffraction spectra of x-rays of TiO_2/CuO sample with a Concentration of 5 wt.% CuO.

TiO_2/CuO (90:10) exhibits the same behaviour as the TiO_2/CuO (95:5). The single peak of anatase TiO_2 (211) disappears. The intensity of all peaks associated with monoclinic CuO increases because of the change in its ratio. The intensity of anatase TiO_2 with the (111) plane decreases at 2θ of 40°.

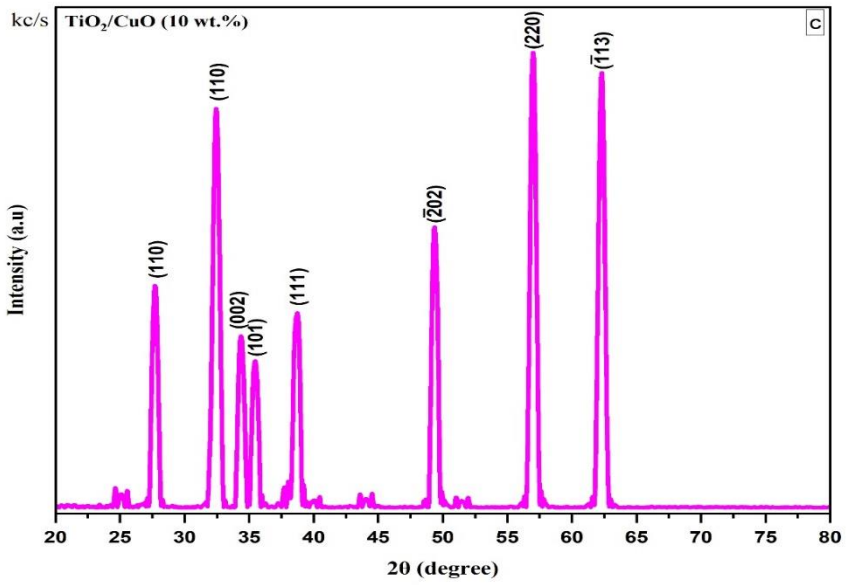

Figure (4.3) Diffraction spectra of x-rays of TiO_2/CuO sample with a Concentration of 10 wt.% CuO.

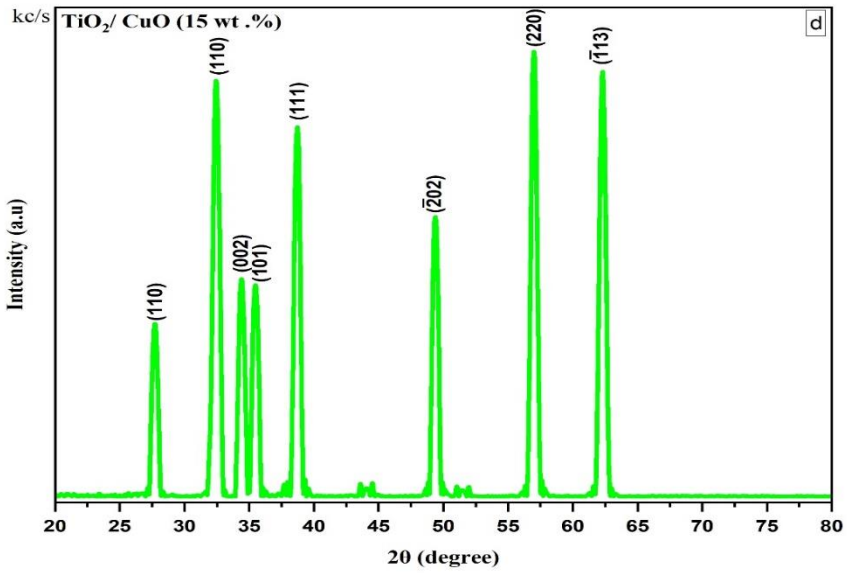

Figure (4.4) Diffraction spectra of x-rays of TiO_2/CuO sample with a Concentration of 15 wt.% CuO.

TiO_2/CuO (85:15) exhibits the disappearance of anatase TiO_2 with the (111) plane at 2θ of 40° with an increase in all peaks associated with monoclinic CuO. Further examination to assess the effect of varying CuO concentrations of TiO_2/CuO via XRD (Figures 4.1–4.6) indicates that TiO_2/CuO with different CuO concentrations show slightly varying XRD patterns.

No new compounds (secondary or tertiary) were formed even with the addition of CuO to TiO_2 with an 85:15 weight ratio.

TiO_2/CuO (85:15) exhibits diffraction peaks characteristic of monoclinic CuO at 35.48° and 38.73°, which are attributed to a high CuO concentration, corresponding to the (002) and (111) planes, respectively. The peak intensity of anatase TiO_2 diminishes, indicating that TiO_2 and CuO coexist at the TiO_2/CuO heterojunction, as reported. Hanaor and Sorrell (2011) indicated that the existence of anatase and rutile TiO_2 phases in a sample with a high CuO concentration encouraged the transformation of anatase to rutile TiO_2.

A high concentration of 15 wt.% CuO loading exhibits the presence of rutile TiO_2 owing to its higher stability than anatase TiO_2. Figure 4.4 illustrates the presence of rutile TiO_2 in TiO_2/CuO (85:15) with peaks at 2θ values of 27.40° and 57.07°, corresponding to the (110) and (220) planes. Conversely, the peaks at 2θ values of 49.0° and 55.05° attributed to the (200) and (105) anatase TiO_2 are absent. These data indicate that as the concentration of CuO increases, the intensity of the XRD peak increases and the corresponding FWHM decreases. Thus, the crystal quality of the TiO_2/CuO nanocomposite improves without any phase changes. The Debye–Scherrer equation calculates the average crystal size across all samples and can be determined by analysing the 2θ values from the XRD data [Eq. (4.2)].

$$D = \frac{K\lambda}{\beta \cos\theta} \qquad (4.2)$$

D is the average size of crystallites with the Scherrer constant k fixed at 0.9, λ is 0.15406 nm representing the wavelength of the X-ray beam, and β represents the FWHM. Crystallite size is influenced by lattice micro-strain and peak intensity.

Typically, as the CuO concentration increases, the average crystallite size diminishes, potentially because of the growth of the crystal structure.

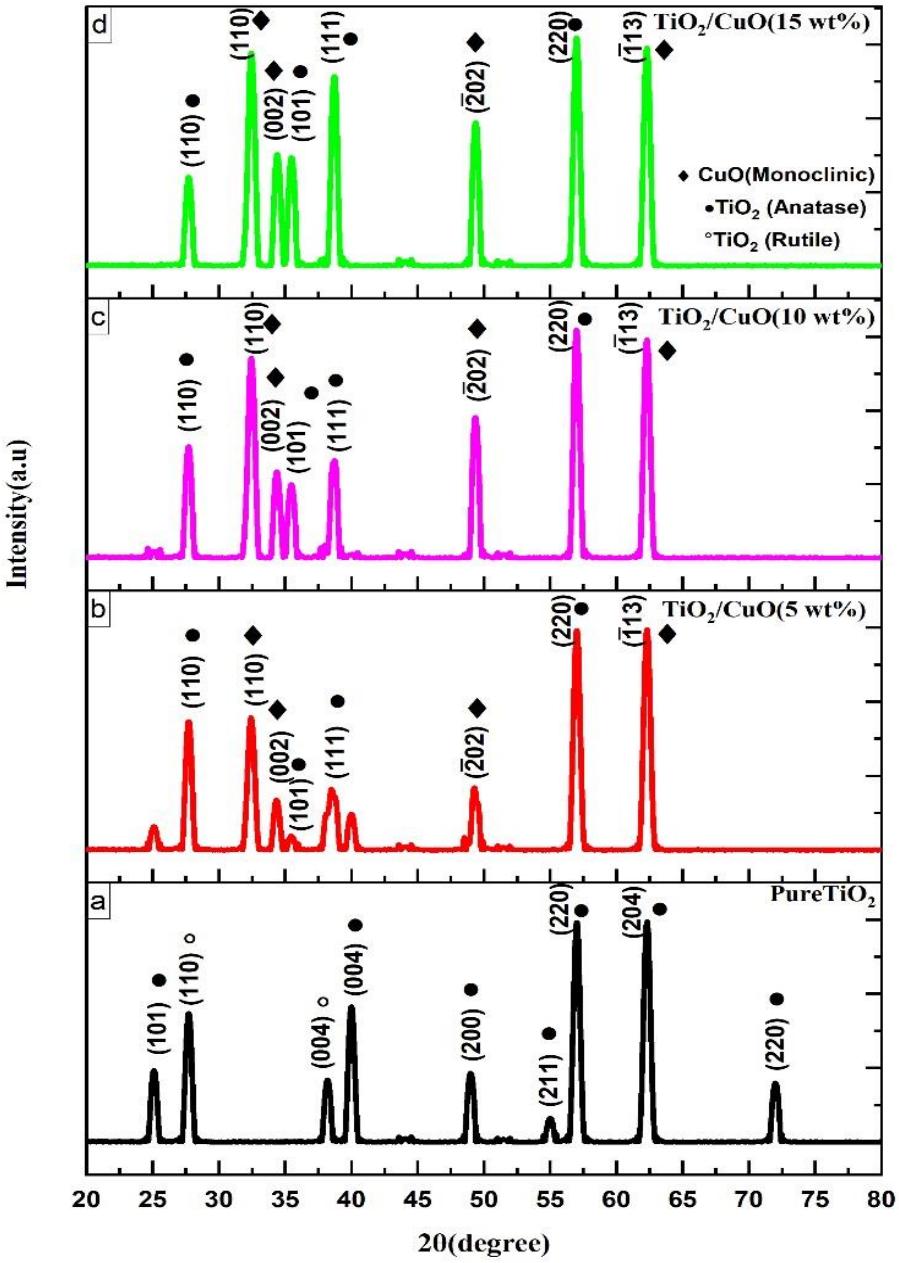

Figure (4.5) XRD spectra for nanocrystalline TiO_2/CuO samples with a concentration as (a) pure TiO_2, (b)TiO_2/CuO (5 wt.% CuO), (c) TiO_2/CuO (10 wt.% CuO), (d) TiO_2/CuO (15 wt.% CuO).

Table 4. 2 XRD Data

2 θ Pure	**Intensity**	**hkl**	**2 θ (5wt %)**	**hkl**	**Intensity**	**2 θ (10wt %)**	**Intensity**	**2 θ (15wt %)**	**Intensity**
25.1A	308.1472	101	27.72	101	555.1586	27.7	377.3056	27.72	300.1748
27.72R	555.2127	110	32.42	110	571.7071	32.44	677.922	32.44	723.0469
38.2R	267.9113	004	34.36	002	216.0613	34.36	291.6687	34.4	377.8395
40A	584.4377	004	38.48	101	261.2815	35.46	249.3755	35.48	367.6487
49A	297.6506	200	38.76	111	229.7686	38.72	330.5968	38.72	642.0048
57.02R	946.7274	220	49.28	-202	269.4646	49.36	476.6409	49.38	485.7967
62.32A	950.5576	204	57.02	220	947.1461	57	773.0342	57	773.0342
72A	254.7696	220	62.32	-113	950.5576	62.3	738.6433	62.3	738.6433

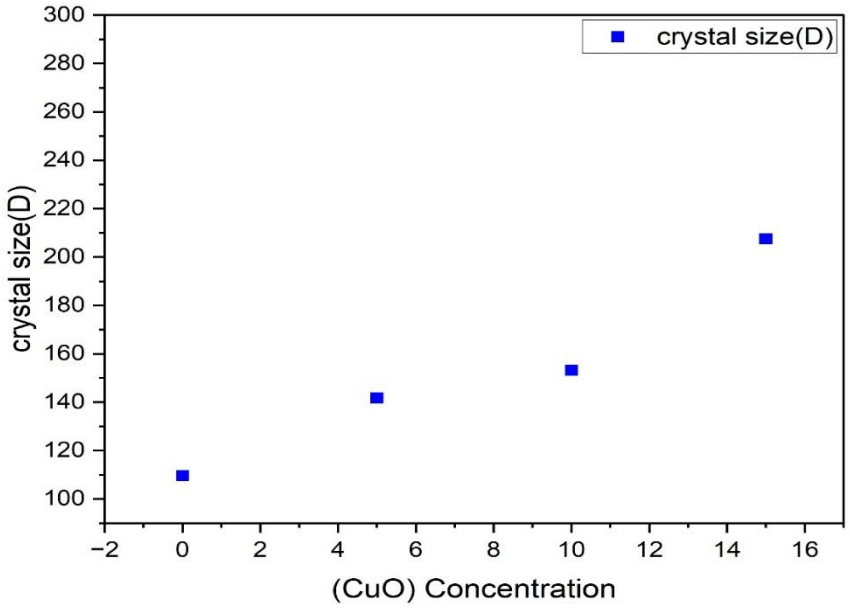

Figure (4.6) Behaviour of the crystal size with the CuO concentration.

Table 4.3 XRD parameters for the samples at different CuO concentrations

Samples of TiO_2 with different concentrations of CuO	2 θ (º) (peak position)	FWHM (β_{hkl})	crystallite size D (nm)
pure	62.3108	0.75	109.62
5%	62.3108	0.58	141.75
10%	62.31079	0.501	153.21
15%	56.99612	0.41	207.53

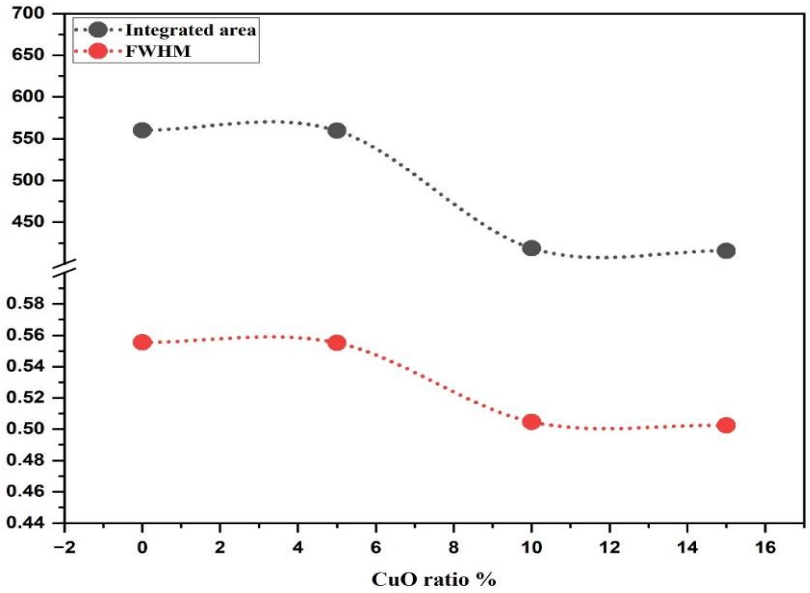

Figure (4.7) The effect of CuO ratio on the (a) FWHM and (b) the Integrated intensity

Figure 4.7 demonstrates that the integrated intensity decreases gradually as the CuO ratio increases, providing evidence of the characteristics of nanocomposite ordering samples. This enhanced order is attributed to the atom arrangement caused by CuO doping, which reduces entanglements per atom and a consequential increase in atom mobility. Conversely, the reduction in overall intensity signals an enhancement in the number of ordered phases present within the samples. This decrease is indicative

of improved crystallinity. The data indicates that an increase in CuO ratios reduces the FWHM, which suggests an increase in crystal size (Figure 4.7). The Debye–Scherrer equation determines the average crystalline size of all samples based on the XRD data. The average grain size increases from 100.9 nm to 207.3 nm as the CuO concentrations increase.

4.3 Chemical Structure

The FTIR analysis of the samples was conducted to examine the structure modifications of TiO_2/CuO with different CuO concentrations (5 wt.%, 10 wt.% and 15 wt.%, Figure 4.8). The changes were assessed based on the relative rise or fall in peak intensity of the functional groups in the TiO_2/CuO composites. The absorbance variation measured at these characteristic wavenumbers with different CuO concentrations indicates the characteristic transmittance peaks of TiO_2/CuO. The pure TiO_2 spectrum shows the characteristic bands at 443.63, 879.54 and 1433 cm^{-1} , which are ascribed to Ti–O–Ti vibration. The broad absorption peak at ~3400 cm^{-1} is owing to OH bending vibrations attached to Ti. The spectra of TiO_2/CuO with different CuO concentrations lie between TiO_2 and CuO bands. The bands at 536.21, 487.99 and 453.27 cm^{-1} are assigned to CuO vibrations. Figures show that the characteristic bands of CuO increase with increasing CuO concentrations, similar to the XRD results.

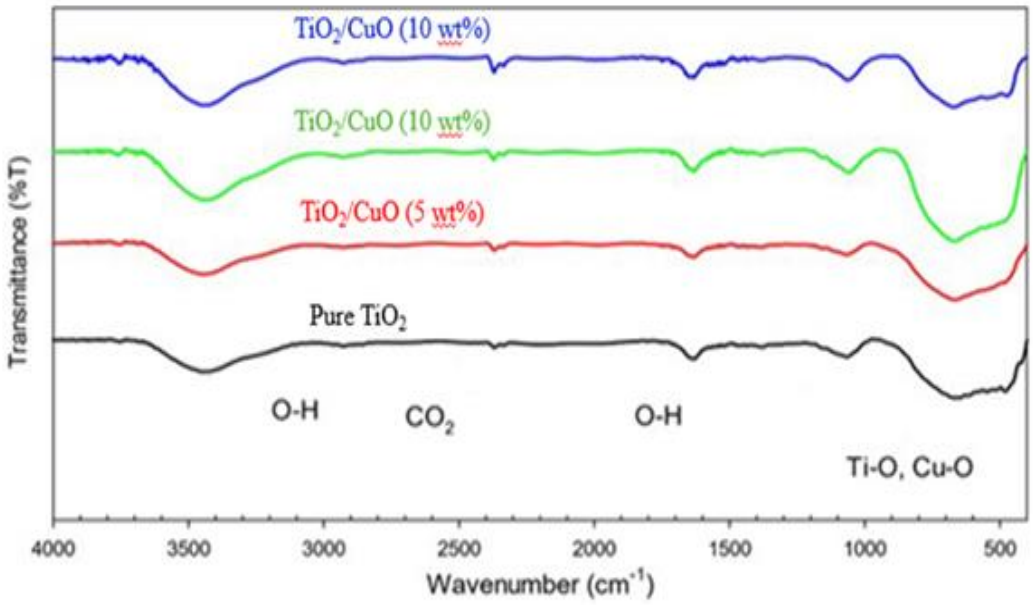

Figure (4.8) FTIR spectra (Transmittance vs. wavenumbers) of the TiO_2/CuO nanocomposite %),d) with a Concentration as: a) pure TiO_2, b) TiO_2/CuO (5wt %), c) TiO_2/CuO(10 wt TiO_2/CuO(15wt %).

4.4 Optical Analysis of TiO_2/CuO

4.4.1 Scan Electron Microscope (SEM)

The morphology of TiO_2/CuO was characterised via SEM. Figure 4.9 shows that TiO_2/CuO differs relatively. However, it generally comprises irregular spherical particles and microstructures in the gaps of these particles. An image of TiO_2/CuO displays grey particles with a distinct microstructure. The white particles suggest the presence of TiO_2, while the grey particles signify Cu-doped TiO_2. The addition of Cu dopants increases the particle size of the samples more than that of pure TiO_2. An increase in the particle size indicates enhanced photocatalytic activity.

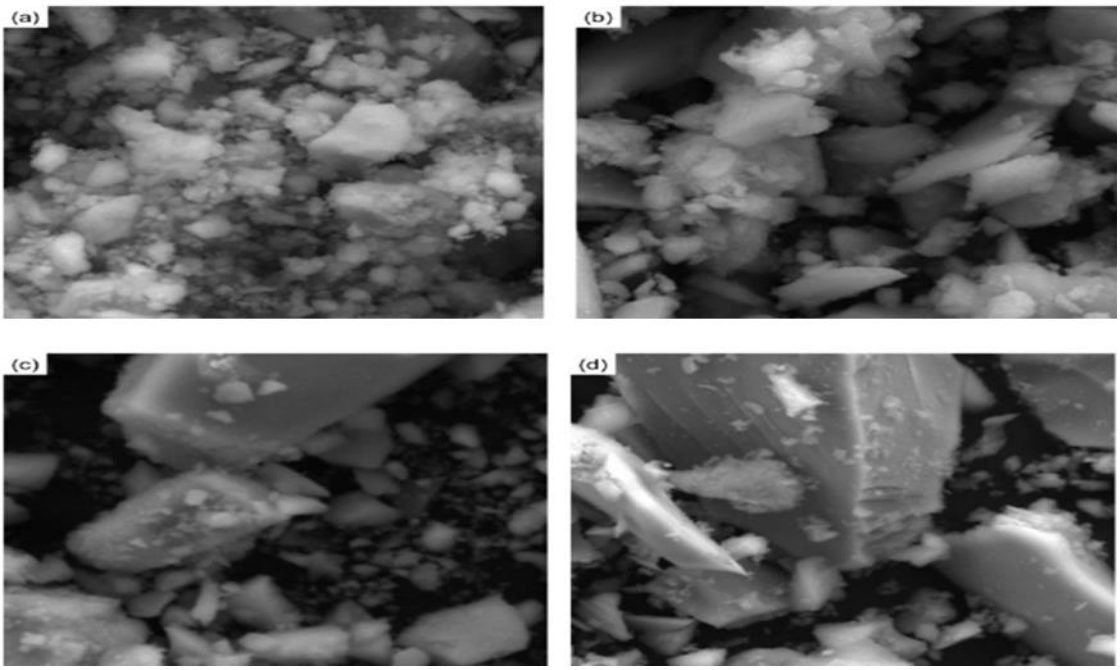

Figure (4.9) SEM morphology of (a) pure TiO_2, (b) TiO_2/CuO (5 wt.%), (c) TiO_2/CuO (10 wt.%) and (d) TiO_2/CuO (15 wt.%)

4.4.2 Effect of the CuO Concentration on Absorption and UV Reflectance

We investigated the optical properties of the synthesised nanocomposites in the wavelength range of 300–800 nm. Figures 4.10–4.19 show the absorption spectra of TiO_2/CuO providing significant insights into the composition and energy gap of nanocomposites. Optical absorption measurements were conducted to investigate the impact of different CuO concentrations in TiO_2/CuO.

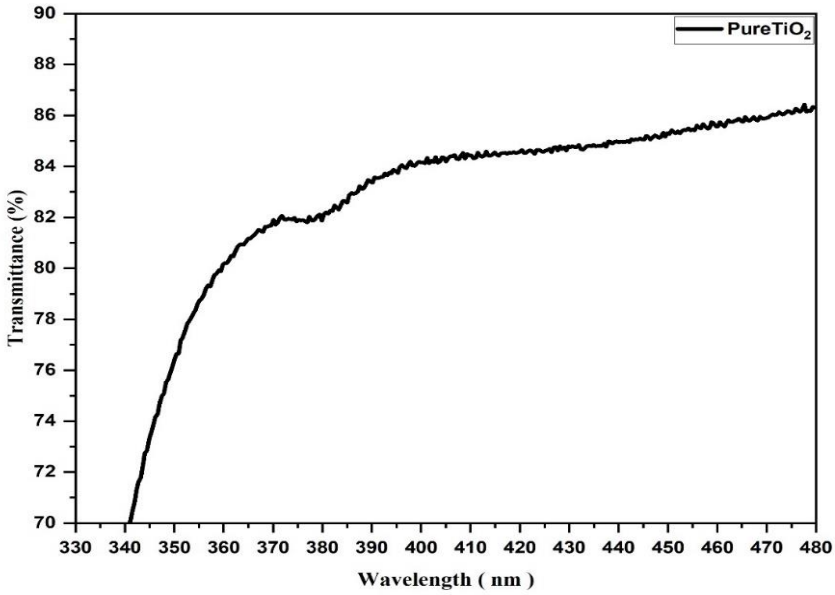

Figure (4.10) Spectral measurements of the transmittance T(λ) of samples measured at room temperature for concentration Pure TiO_2.

Figure (4.10) shows the relation between the transmittance percentage and the wavelength. We find the maximum transmittance value at wavelength 375.5 nm with a transmittance intensity of 81.6%.

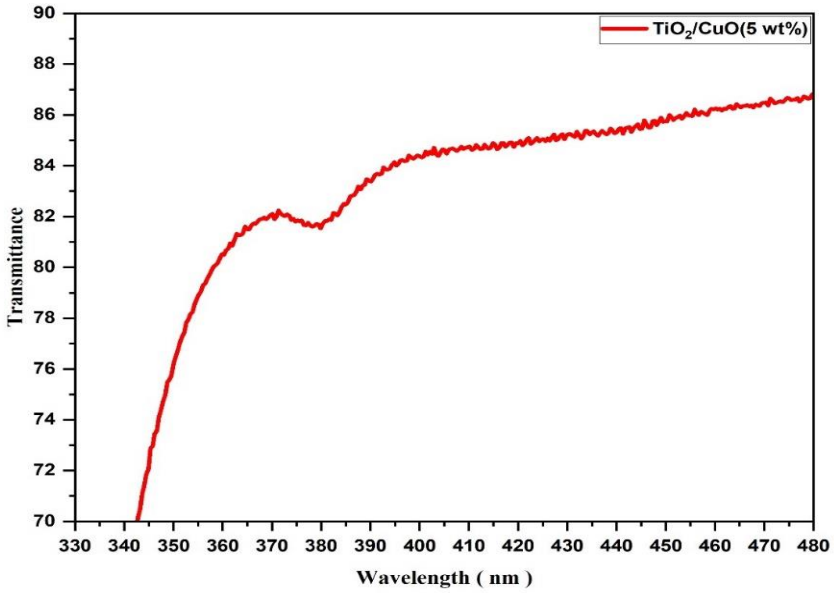

Figure (4.11) Spectral measurements of the transmittance T(λ) of samples measured at room temperature for concentration TiO_2/CuO (5wt%).

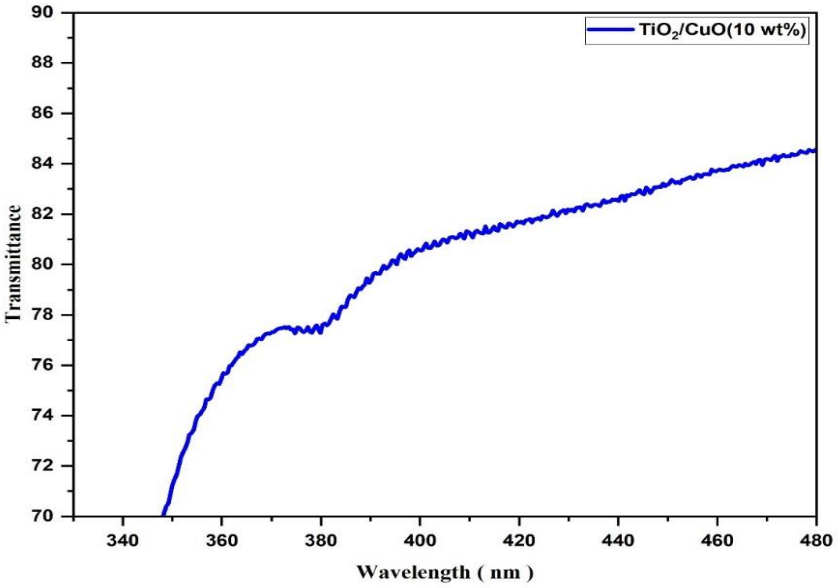

Figure (4.12) Spectral measurements of the transmittance T(λ) of samples measured at room temperature for concentration TiO_2/CuO (10wt%).

From the figure (4.11) we show the relationship between the transmittance percentage and the wavelength, and we find the maximum transmittance value at wavelength 376.3 nm with a transmittance intensity of 77.4 %.

From the figure (4.12), we show the relation between the transmittance percentage and the wavelength, and we find the maximum transmittance value at a wavelength of 377.7 nm with a transmittance intensity of 77.4 %.

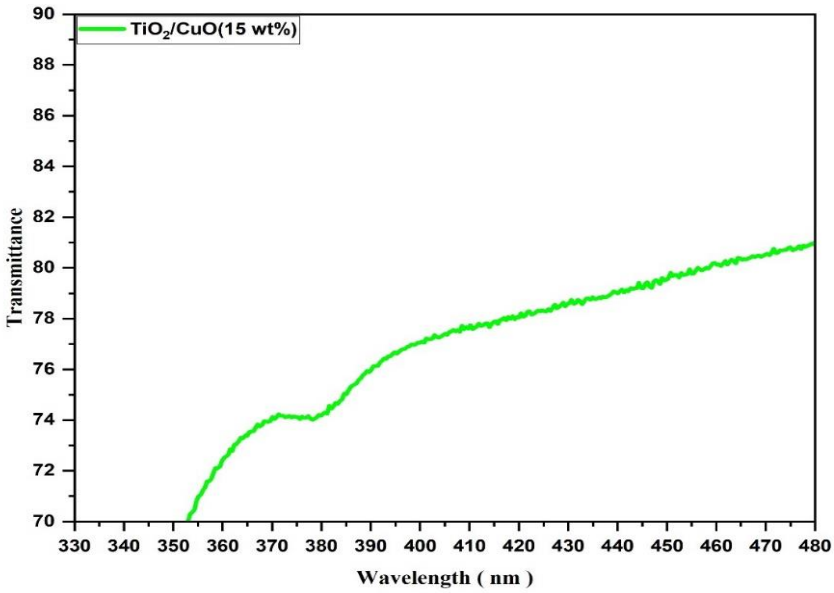

Figure (4.13) Spectral measurements of the transmittance T(λ) of samples measured at room temperature for concentration TiO_2/CuO (15wt%).

From the figure (4.13), we show the relation between the transmittance percentage and the wavelength, and we find the maximum transmittance value at a wavelength of 378.11nm with a transmittance intensity of 73.8 %.

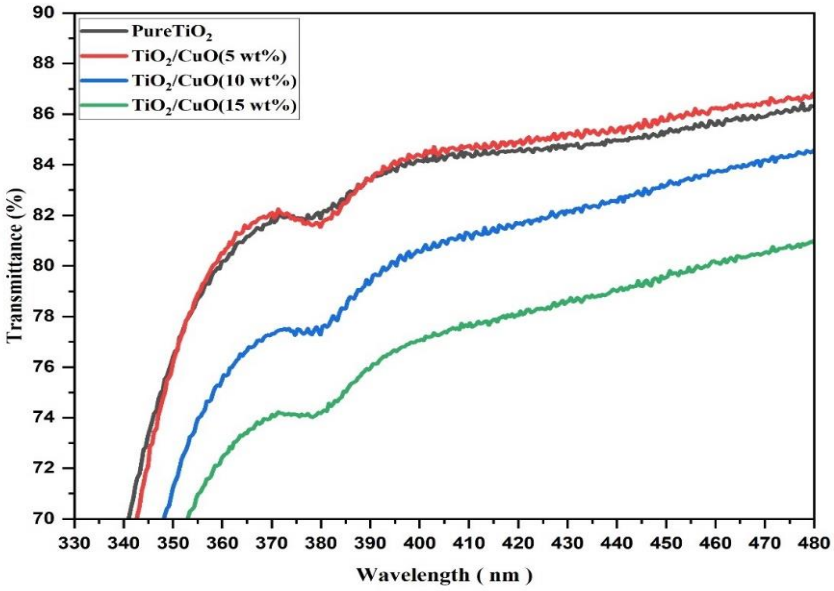

Figure (4.14) Spectral measurements of the transmittance T(λ) of samples measured at room temperature for concentration (a)Pure TiO_2, (b)TiO_2/CuO (5wt%), (c)TiO_2/CuO (10wt%), and (d) TiO_2/CuO 15wt%).

Figure 4.14 shows the relation between transmittance percentage and wavelength, and the maximum transmittance value of the 423nm wavelength exhibits a transmittance intensity of 84%.

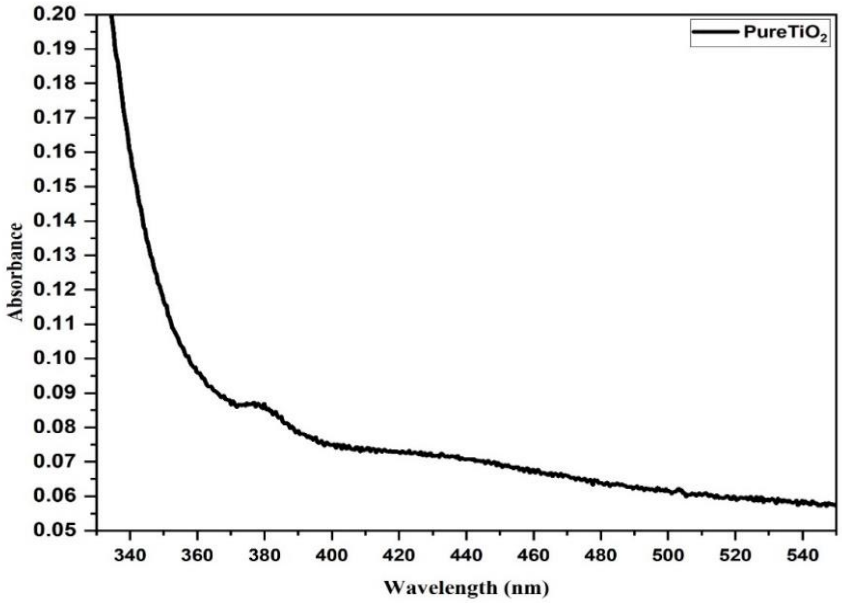

Figure (4.15) Spectral measurements of Absorbance (a.u) of samples measured at room temperature for concentration ((a)TiO_2 pure).

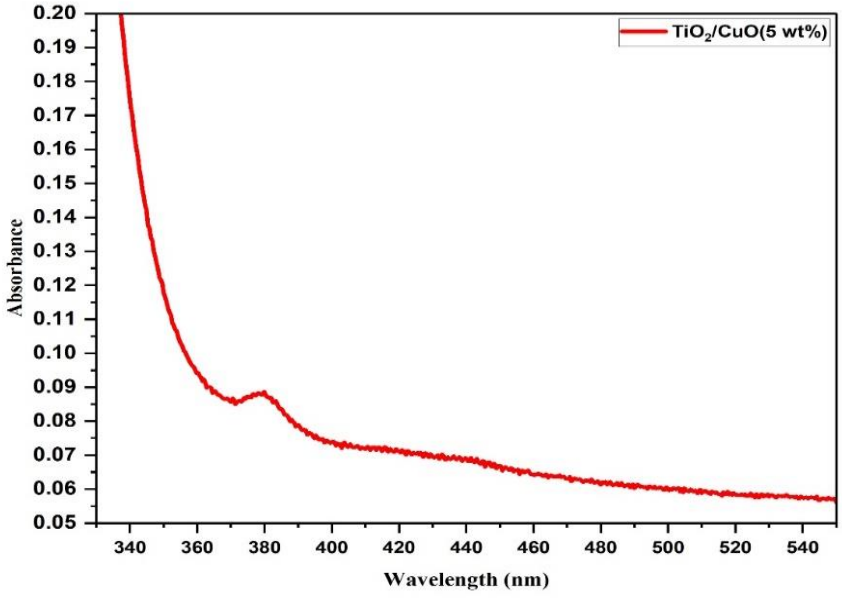

Figure (4.16) Spectral measurements of Absorbance A(λ) of samples measured at room temperature for concentration (b) TiO_2/CuO (5 wt%).

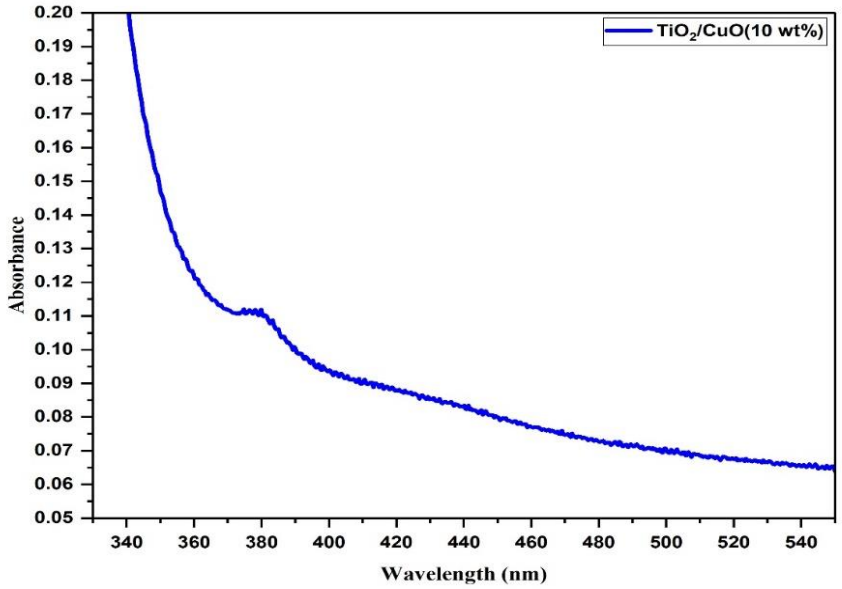

Figure (4.17) Spectral measurements of Absorbance A(λ) of samples measured at room temperature for concentration (c) TiO_2/CuO (10 wt%).

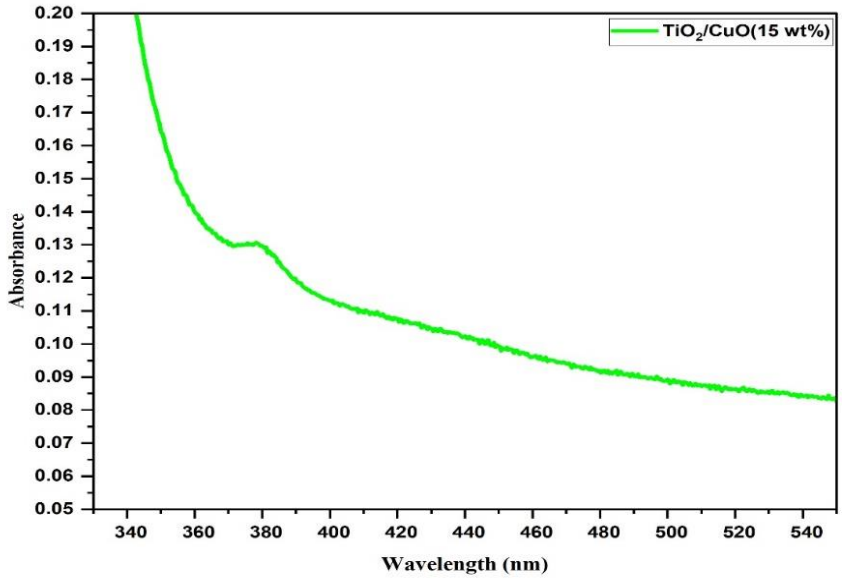

Figure (4.18) Spectral measurements of Absorbance A(λ) of samples measured at room temperature for concentration (d) (TiO_2/CuO (15 wt%).

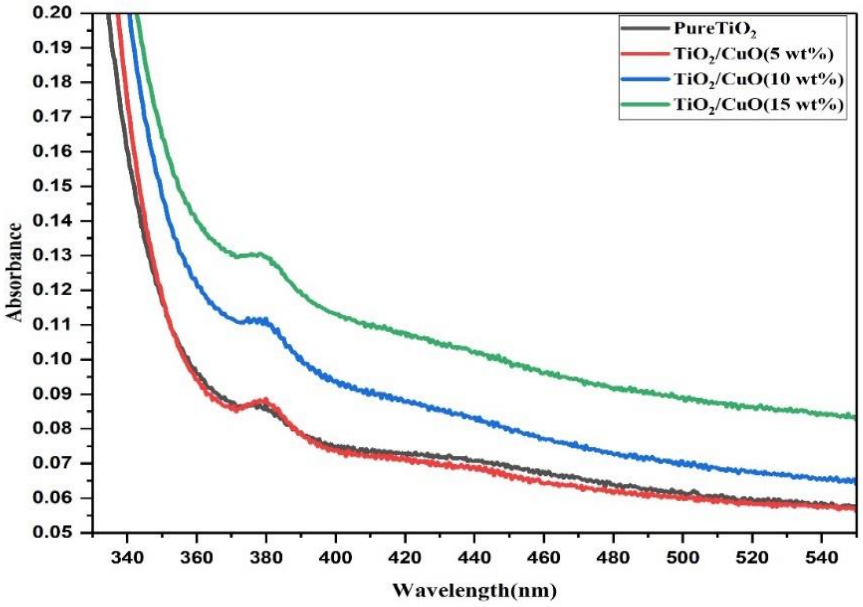

Figure (4.19) Spectral measurements of Absorbance A(λ) of samples measured at room temperature for concentration (a) Pure TiO_2, (b)TiO_2/CuO(5wt%), (c)TiO_2/CuO (10 wt%), and (d) TiO_2/CuO (15 wt%).

All samples in Figure 4.19 exhibit a sharp absorption band in the region of wavelengths <350 nm. Figure 4.19 shows an increase in the maximum intensity of the absorbance (A) percentage with a shift from a low wavelength (327.413 nm) to a high wavelength (414.88 nm) with an absorption edge energy value of 3.78–2.98 eV as the concentration increases from 2 μm to 8 μm. This redshift indicates that the concentration has a strong effect on optical parameters. The increasing intensity of absorption energy with the increasing thickness of the thin films indicates consequent lowering of the optical energy bandgap value.

4.4.3 Impact of Concentration on the Optical Energy Band Gap

Determining the optical absorption coefficient for thin films is crucial for understanding the amount of light absorbed, particularly in the regions of strong absorption where high light intensities can penetrate. The absorption coefficient can be calculated using Eq. (4.4).

$$\alpha = \frac{2.303 * A}{t} \qquad (4.4)$$

where A and t are the concentration and absorption of the sample, respectively. The excitation of the electron from E_V to E_C essentially causes absorption.

The Tauc relation was used to find the optical energy gap of TiO_2 and TiO_2/CuO, which can be expressed using Eq. (4.5).

$$\alpha h\upsilon = \beta(h\upsilon - E_g^{\ x}) \qquad (4.5)$$

Here, α is the absorption coefficient, β is the constant related to electronic transition probabilities, hν indicates the energy of the photon, Eg is the optical forbidden gap, and x is a factor that dictates the type of electronic transition possible during photon absorption. The values for direct transitions are as mentioned: forbidden x = 3/2 and allowed x = 1/2. In contrast, for indirect transitions x = 2 and 3. The Tauc equation shows that the optical energy gap can be derived by plotting $(\alpha h\nu)^{(1/2)}$ versus hν. This analysis focuses on the linear segment of the fundamental absorption edge observed in the UV–Vis absorption spectra, as demonstrated in Figures 4.20–4.24. By extrapolating the linear segment to the hν axis, we can determine the associated indirect bandgap. The obtained values are plotted as a function of the CuO concentration in Figure 4.23. The optical energy gap values decrease with the increasing CuO concentration from 3.2 eV (control sample) to 2.95 eV (composite samples).

Table 4. 4 Energy bandgap and for samples at a different Concentration of CuO (5 wt %, 10 wt %, and 15 wt %).

Concentration (%)	E_g (eV)
Pure TiO_2	3.2
TiO2/CuO(0.05wt%)	3.186
TiO2/CuO(0.1wt%)	3.04
TiO2/CuO(0.15wt%)	2.95

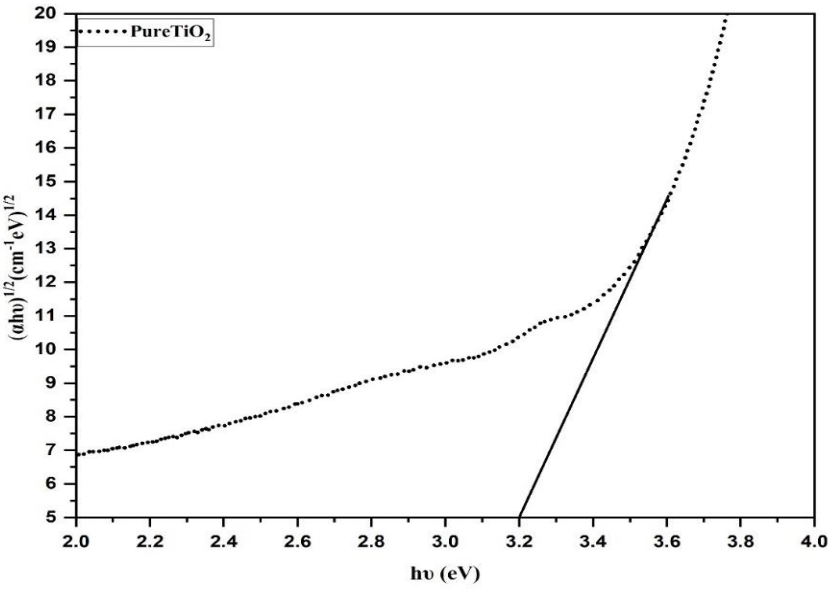

Figure (4.20) E_g of (a) (Pure TiO_2).

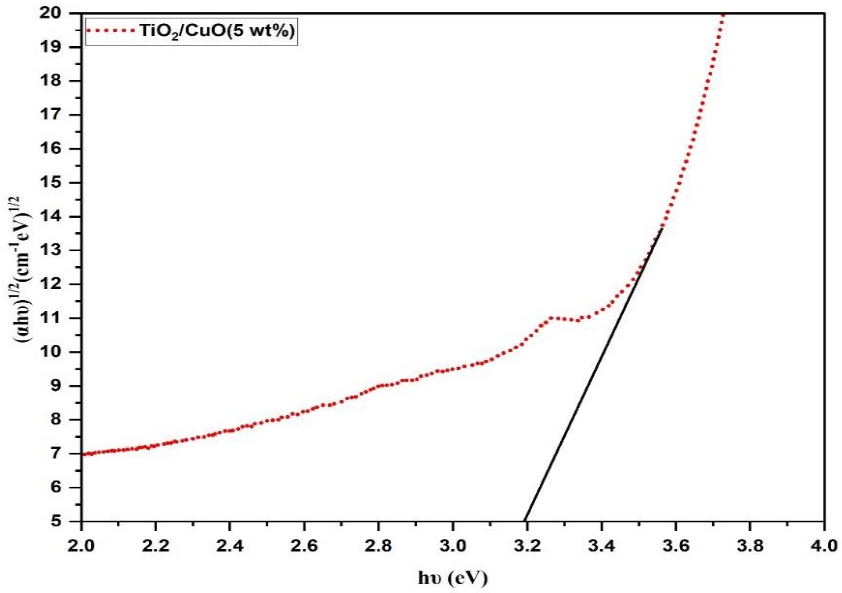

Figure (4.21) E_g of (b)TiO_2/CuO (5 wt.%).

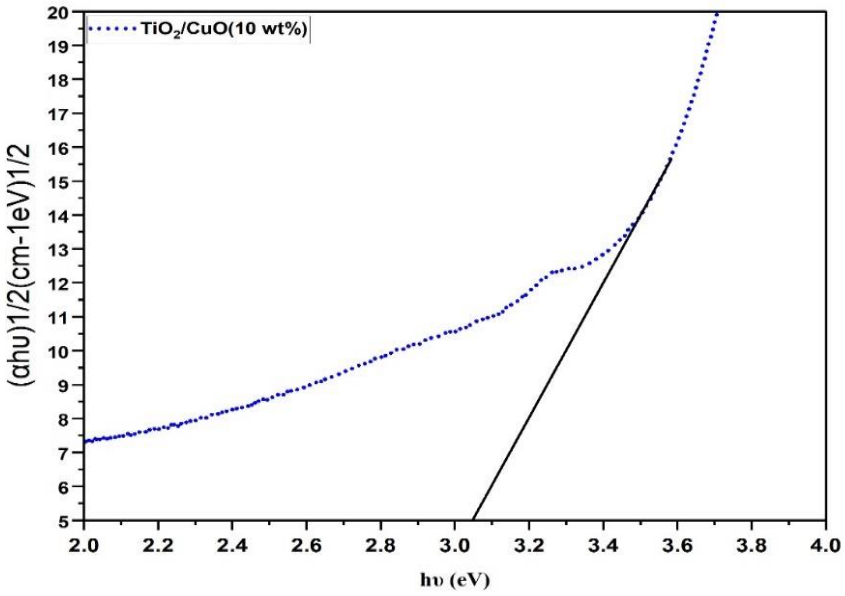

Figure (4.22) E_g of (c)TiO_2/CuO (10 wt.%).

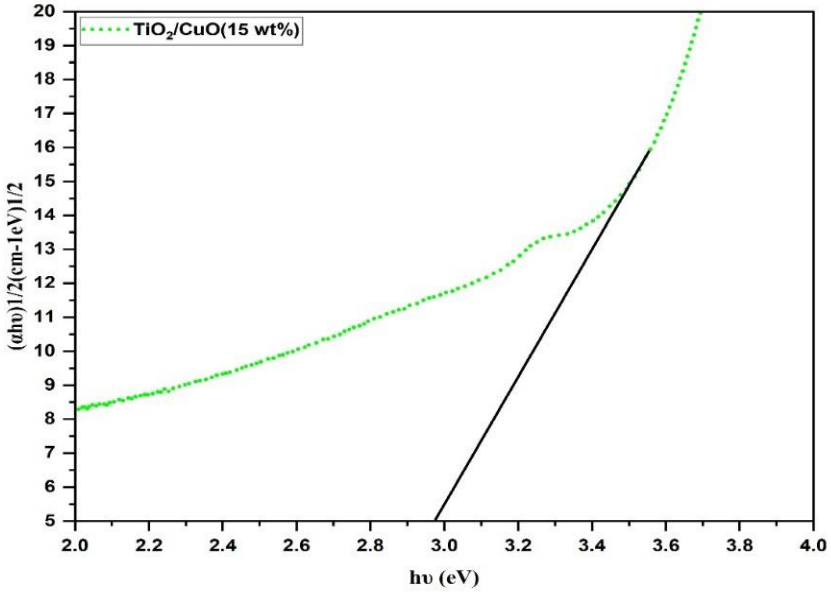

Figure (4.23) E_g of (d)TiO_2/CuO (15 wt.%).

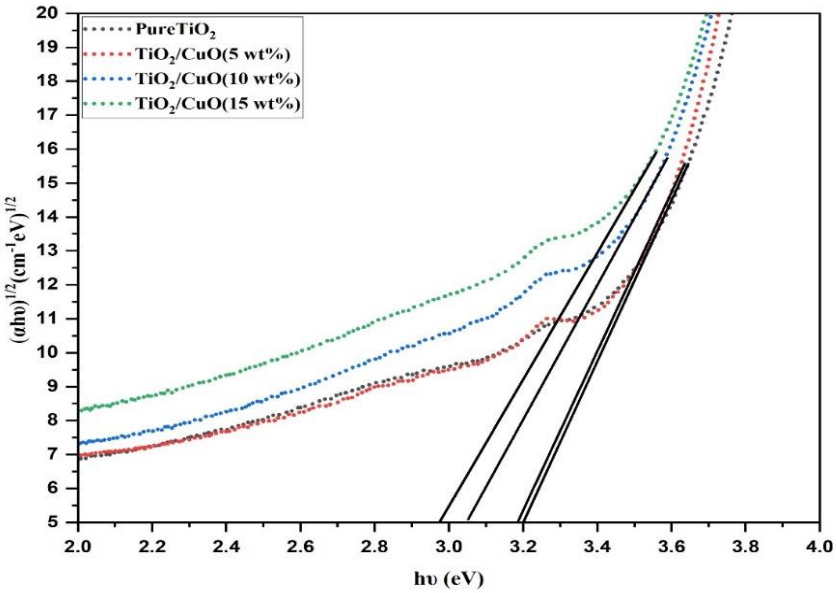

Figure (4.24) E_g values for samples with a concentration (a)Pure TiO_2, (b)TiO_2/CuO (5 wt%), (c)TiO_2/CuO (10 wt%), and (d) TiO_2/CuO (15 wt%).

4.4.4 Effect of the Skin Depth.

The graph presented in Figure 4.25 shows that pure TiO_2 has a skin depth that first increases from 300 to 350 nm and then decreases. Its lowest point is ~379.48 nm, following which it increases, reaching a maximum of 678.52 nm. This shows that electromagnetic radiation with a wavelength of ~800 nm penetrates the material deeply.

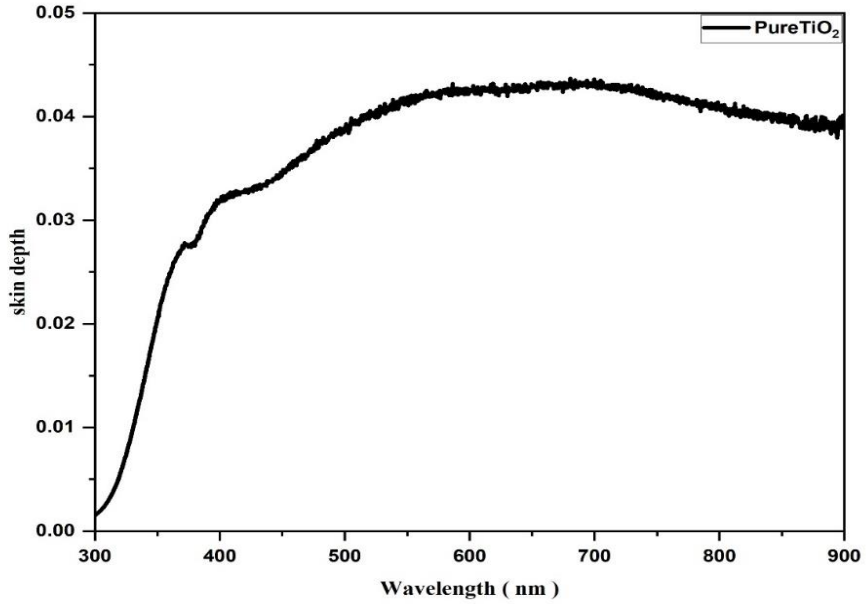

Figure (4.25) a graph showing how skin depth varies with wavelength.

Figure 4.26 shows that the skin depth of TiO_2/CuO (5 wt.%) initially increases up to 370.7 nm and then decreases. The minimum value of skin depth is ~379.48 nm before it increases again, reaching a maximum of 678.52 nm. This indicates that electromagnetic radiation of ~678.52 nm penetrates the material effectively.

Figure 4.27 shows that the skin depth of TiO_2/CuO (10 wt.%) initially increases to 369.2 nm before decreasing. The minimum skin depth occurs at ~380.1 nm, after which it increases again, reaching a maximum of 610 nm. This indicates that

electromagnetic radiation with a wavelength of ~610 nm penetrates the material deeply.

Figure 4.28 shows that the skin depth of TiO_2/CuO (15 wt.%) initially increases up to 370 nm and then decreases. The minimum value of skin depth is ~379.48 nm, after which it increases again with a maximum of 568.05 nm. This shows that electromagnetic radiation with a wavelength of ~568.05 nm penetrates the material deeply.

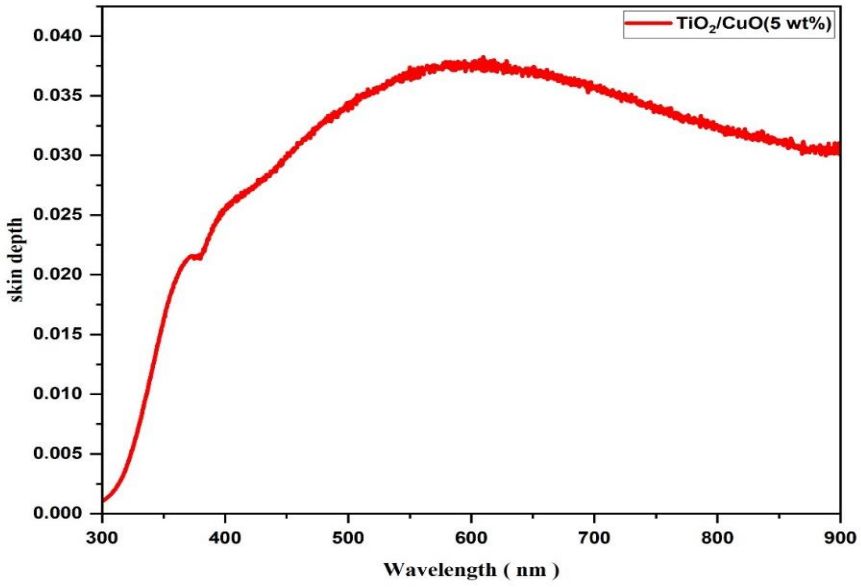

Figure (4.26) a graph showing how skin depth varies with wavelength.

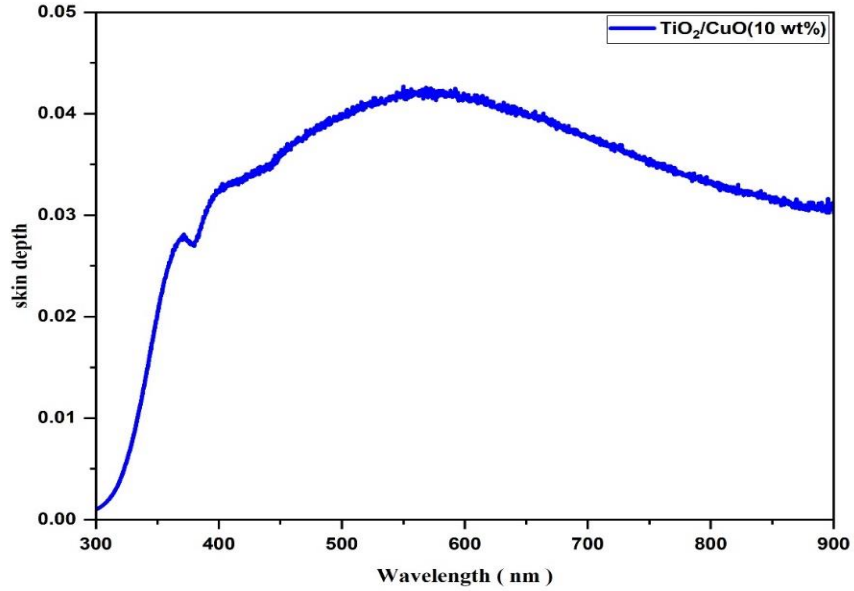

Figure (4.27) a graph showing how skin depth varies with wavelength..

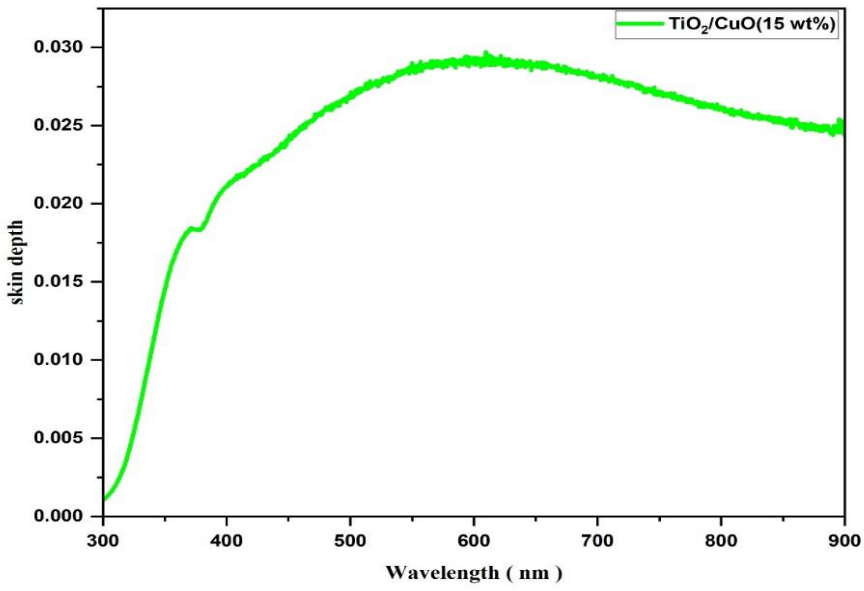

Figure (4.28) a graph showing how skin depth varies with wavelength.

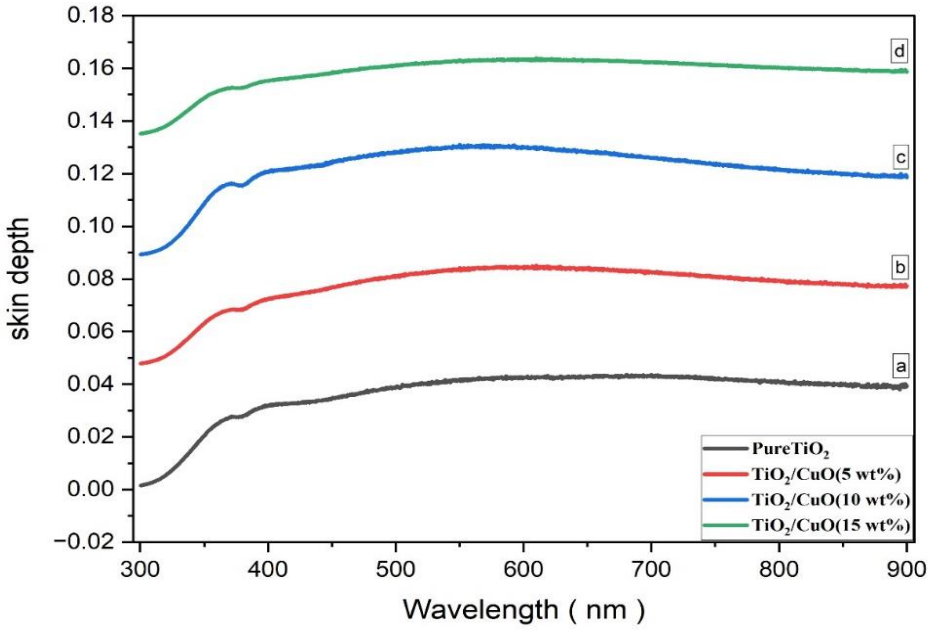

Figure (4.29) a graph showing how skin depth varies with wavelength..

Figure 4.29 shows that the skin depth initially increases up to 370.7 nm and then decreases. The minimum value of skin depth is ~377.8 nm before it increases again, reaching a maximum of 609.86 nm. This indicates that electromagnetic radiation with a wavelength of ~609.86 nm penetrates the material deeply.

4.4.5 Effect of the Refractive Index.

The refractive index of a semiconductor indicates how transparent it is to incoming spectral radiation. Evaluating the refractive index of optical materials is crucial for integrated optic devices. The refractive index (n) of the samples prepared was determined using the equations provided below. [Eq. (4.6)].

$$n = \frac{1+\mathrm{R}}{1-\mathrm{R}} + \sqrt{\frac{4R}{(1-R)^2} - K^2} \qquad (4.6)$$

Figures 4.30-4.34 illustrate the refractive index (n) for both pure TiO_2 and TiO_2/CuO nanoparticle samples. The graph indicates the refractive index of the pure TiO_2 nanoparticles.

The refractive index of TiO_2 (titanium dioxide) generally ranges from 1.38 to 1.4 for amorphous TiO_2, depending on density, 2.49 for anatase, and approximately 2.80 for rutile. In contrast, CuO (copper(II) oxide) has a lower refractive index of about 0.86. The elevated refractive index of TiO_2 makes it suitable for applications such as waveguides and Bragg mirrors. Furthermore, the significant difference in refractive indices between TiO_2 and CuO can be leveraged for structural color applications.

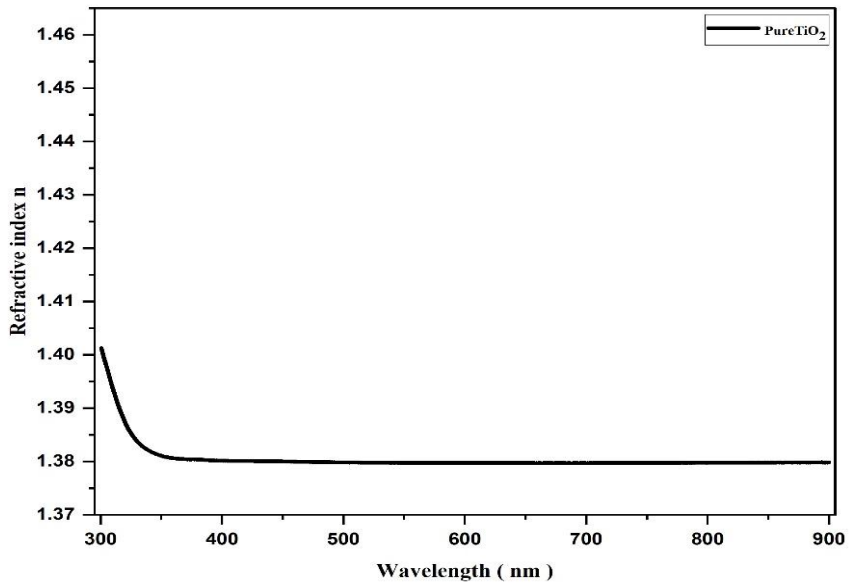

Figure (4.30) Refractive index (n) vs. the wavelength of (a) pure TiO_2.

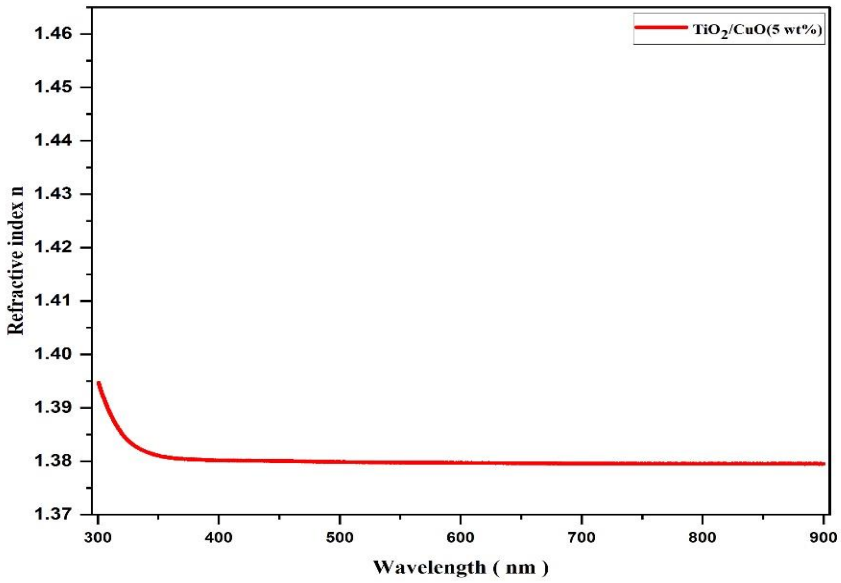

Figure (4.31) Refractive index (n) vs. the wavelength of (b) TiO_2/CuO (5 wt.%)

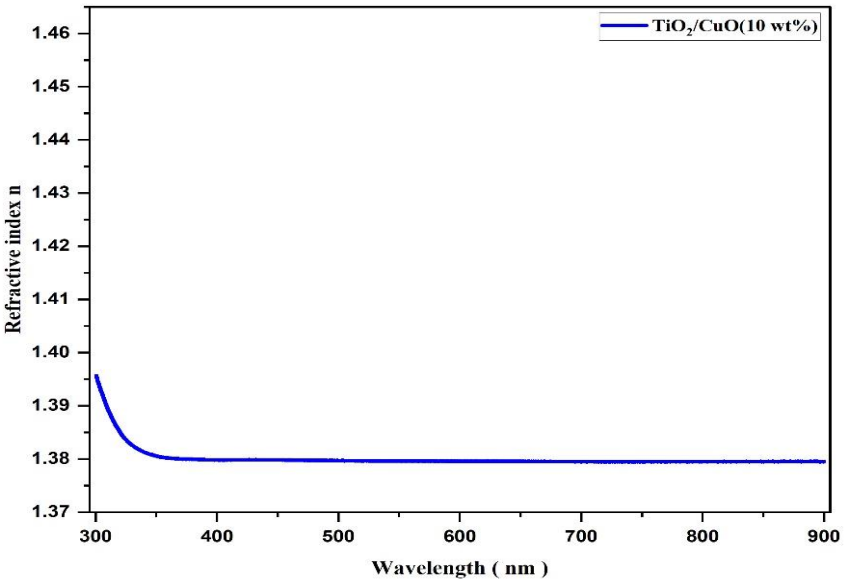

Figure (4.32) Refractive index (n) vs. the wavelength of (c) TiO_2/CuO (10 wt.%)

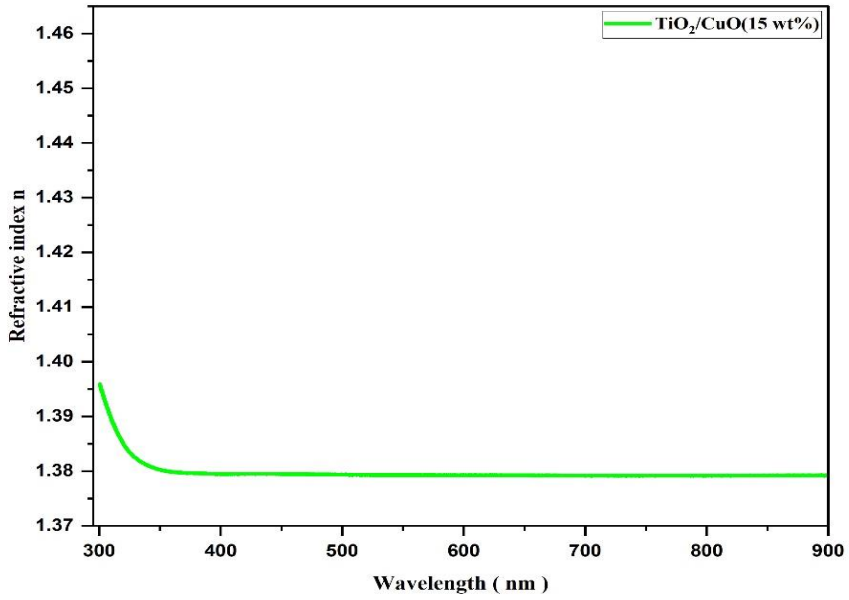

Figure (4.33) Refractive index (n) vs. the wavelength of (d) TiO_2/CuO (15 wt.%)

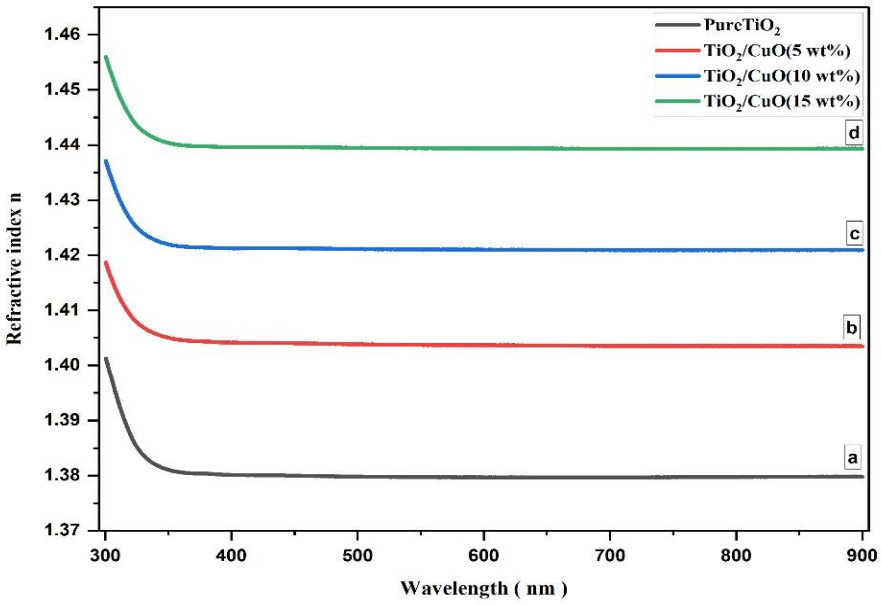

Figure (4.34) Refractive index (n) vs. the wavelength of (a) Pure TiO_2, (b) TiO_2/CuO (5 wt.%), (c) TiO_2/CuO (10 wt.%), and (d) TiO_2/CuO (15 wt.%)

4.5 Conclusion

The development of optoelectronic and solar cells with novel structures as substitutes for commercial applications is an important area. The TiO_2/CuO nanocomposite is considered a promising choice for the cost-effective development of reliable solar energy devices for increasing their efficiency. TiO_2/CuO was prepared using the sol–gel method. The CuO concentration significantly impacted the structure and optical properties of the nanocomposites. The XRD results of the samples revealed anatase and rutile phases of TiO_2, while a monoclinic CuO phase was present. The average crystallite size increases with a high ratio of CuO (5 wt.%, 10 wt.% and 15 wt.%). UV–vis spectral results indicated that increasing the CuO concentration in TiO_2/CuO exhibited a redshift, indicating that the TiO_2:CuO ratio strongly affected the optical parameters. The maximum intensity of the absorbance percentage increased with a shift from a low wavelength to high wavelength with absorption edge energy values (3.2–2.98) eV as the CuO concentration increased from 5 wt.% up to 15 wt.%. A high wavelength means a low energy transmittance from nanocomposites, indicating an increase in absorbed energy. The optical energy gap decreased because of the formation of a light state during sample preparation. An examination of the effect of concentration on optical parameters revealed that increasing the CuO ratio enhanced its optical activity and shifted it to the visible region, useful in photocatalytic and energy-saving applications.

References

[1] Z. Dilli, A. Akturk, N. Goldsman, M. A. Holloway, and J. C. Rodgers, "Nonlinear behavior of electrostatic discharge protection structures under high-power microwave excitation: Modeling and simulation," in *2011 IEEE International Symposium of Circuits and Systems (ISCAS)*, 2011, pp. 1840–1843. doi: 10.1109/ISCAS.2011.5937944.

[2] "OPTICAL AND ELECTRICAL CHARACTERIZATION OF Cd x Se 1-x S AND Cu 2 STHIN FILMS FOR SOLAR CELL APPLICATION MOGUNDE CHARLES MORARO (B.EdSc)," 2016.

[3] A. L. Linsebigler, G. Lu, and J. T. Jr. Yates, "Photocatalysis on TiO2 Surfaces: Principles, Mechanisms, and Selected Results," *Chem Rev*, vol. 95, no. 3, pp. 735–758, 1995, doi: 10.1021/cr00035a013.

[4] M. Dey *et al.*, "Deposition of CdS Thin Film by Thermal Evaporation," in *2019 International Conference on Electrical, Computer and Communication Engineering (ECCE)*, Feb. 2019, pp. 1–5. doi: 10.1109/ECACE.2019.8679325.

[5] B. K. Meyer *et al.*, "Binary copper oxide semiconductors: From materials towards devices," *physica status solidi (b)*, vol. 249, no. 8, pp. 1487–1509, 2012, doi: https://doi.org/10.1002/pssb.201248128.

[6] S. C. Abrahams and J. L. Bernstein, "Rutile: Normal Probability Plot Analysis and Accurate Measurement of Crystal Structure," *J Chem Phys*, vol. 55, no. 7, pp. 3206–3211, Oct. 1971, doi: 10.1063/1.1676569.

[7] M. HORN, C. F. SCHWEBDTFEGER, and E. P. MEAGHER, "Refinement of the structure of anatase at several temperatures," vol. 136, no. 1–6, pp. 273–281, 1972, doi: doi:10.1524/zkri.1972.136.16.273.

[8] P. Sawicka-Chudy *et al.*, "TiO 2 Grown by Pulsed Laser Deposition and Reactive DC Direct Current Sputtering as an Intermediate Buffer Layer in Photovoltaic Structures," *Journal of Nanoelectronics and Optoelectronics*, vol. 13, pp. 995–1000, May 2018, doi: 10.1166/jno.2018.2348.

[9] M. Green, E. Dunlop, J. Hohl-Ebinger, M. Yoshita, N. Kopidakis, and X. Hao, "Solar cell efficiency tables (version 57)," *Progress in Photovoltaics: Research and Applications*, vol. 29, no. 1, pp. 3–15, 2021, doi: https://doi.org/10.1002/pip.3371.

[10] S. Rühle and A. Zaban, “All-oxide Photovoltaics,” in *Advanced Concepts in Photovoltaics*, A. Nozik, G. Conibeer, and M. C. Beard, Eds., The Royal Society of Chemistry, 2014, p. 0. doi: 10.1039/9781849739955-00258.

[11] J. Zheng, S. Bao, and P. Jin, “TiO2(R)/VO2(M)/TiO2(A) multilayer film as smart window: Combination of energy-saving, antifogging and self-cleaning functions,” *Nano Energy*, vol. 11, pp. 136–145, Jan. 2015, doi: 10.1016/J.NANOEN.2014.09.023.

[12] M. C. Rao, R. Koutavarapu, and M. Shekhawat, “Structural and electrical properties of TiO2 thin films,” Mar. 2016, p. 20077. doi: 10.1063/1.4946128.

[13] M. I. Khan, K. A. Bhatti, R. Qindeel, H. S. Althobaiti, and N. Alonizan, “Structural, electrical and optical properties of multilayer TiO2 thin films deposited by sol–gel spin coating,” *Results Phys*, vol. 7, pp. 1437–1439, 2017, doi: https://doi.org/10.1016/j.rinp.2017.03.023.

[14] M. Kang, S. W. Kim, and H. Y. Park, “Optical properties of TiO2 thin films with crystal structure,” *Journal of Physics and Chemistry of Solids*, vol. 123, pp. 266–270, 2018, doi: https://doi.org/10.1016/j.jpcs.2018.08.009.

[15] “a Diagram of the CuO/TiO2 nanostructured composite. The dark and light... | Download Scientific Diagram.” Accessed: May 25, 2025. [Online]. Available: https://www.researchgate.net/figure/a-Diagram-of-the-CuO-TiO2-nanostructured-composite-The-dark-and-light-circles-correspond_fig5_359449635/actions#caption

[16] A. Zaleska, “Doped-TiO 2 : A Review,” 2008.

[17] S. S. Lee, H. Bai, Z. Liu, and D. D. Sun, “Novel-structured electrospun TiO2/CuO composite nanofibers for high efficient photocatalytic cogeneration of clean water and energy from dye wastewater,” *Water Res*, vol. 47, no. 12, pp. 4059–4073, 2013, doi: https://doi.org/10.1016/j.watres.2012.12.044.

[18] S. Rtimi, O. Baghriche, C. Pulgarin, J. C. Lavanchy, and J. Kiwi, “Growth of TiO2/Cu films by HiPIMS for accelerated bacterial loss of viability,” *Surf Coat Technol*, vol. 232, pp. 804–813, Oct. 2013, doi: 10.1016/j.surfcoat.2013.06.102.

[19] A. Tamarani, R. Zainul, and I. Dewata, “Preparation and characterization of XRD nano Cu-TiO $_2$ using sol-gel method,” *J Phys Conf Ser*, vol. 1185, p. 012020, Apr. 2019, doi: 10.1088/1742-6596/1185/1/012020.

[20] P. Sawicka-Chudy, M. Sibiński, E. Rybak-Wilusz, M. Cholewa, G. Wisz, and R. Yavorskyi, "Review of the development of copper oxides with titanium dioxide thin-film solar cells," Jan. 01, 2020, *American Institute of Physics Inc.* doi: 10.1063/1.5125433.

[21] T. Raguram and K. S. Rajni, "Synthesis and characterisation of Cu - Doped TiO2 nanoparticles for DSSC and photocatalytic applications," *Int J Hydrogen Energy*, vol. 47, no. 7, pp. 4674–4689, 2022, doi: https://doi.org/10.1016/j.ijhydene.2021.11.113.

[22] X. YANG, S. WANG, H. SUN, X. WANG, and J. LIAN, "Preparation and photocatalytic performance of Cu-doped TiO2 nanoparticles," *Transactions of Nonferrous Metals Society of China*, vol. 25, no. 2, pp. 504–509, 2015, doi: https://doi.org/10.1016/S1003-6326(15)63631-7.

[23] M. M. Abbas and M. Rasheed, "Solid State Reaction Synthesis and Characterization of Cu doped TiO2Nanomaterials," in *Journal of Physics: Conference Series*, IOP Publishing Ltd, Mar. 2021. doi: 10.1088/1742-6596/1795/1/012059.

[24] Z. Khodair and A. Abd, "Preparation and characterization of structural properties for TiO2 and CuO nanostructures by sol-gel technique," *Mater Today Proc*, vol. 57, Mar. 2022, doi: 10.1016/j.matpr.2022.01.417.

[25] B. Hu, Y. Chen, D. Kong, and Y. Yao, "Large, grid-connected solar photovoltaic power plants renewable energy," *Applied and Computational Engineering*, vol. 7, pp. 375–389, May 2023, doi: 10.54254/2755-2721/7/20230328.

[26] "Solar Systems | supplagent." Accessed: May 13, 2025. [Online]. Available: https://supplagent.com/solar-systems

[27] *Introduction to Solid State Physics Charles Kittel*. 2005.

[28] A. Dobromyslov, "The Regularities of Phase and Structural Transformation in Binary Titanium Alloys with Metals of IV—VIII Groups of the Periodic Table," *Advances in Materials Sciences*, vol. 8, no. 1, Sep. 2008, doi: 10.2478/v10077-008-0004-7.

[29] "Semiconductor Electronics Materials Devices And Simple Circuits - NCERT Book of Class 12 Physics Part II." Accessed: May 25, 2025. [Online]. Available: https://betrained.in/Bihar-Board/12-Physics-Part-II/Semiconductor-Electronics-Materials-Devices-And-Simple-Circuits

[30] "Understanding the Electrical Properties of Conductors, Insulators, and Semiconductors - Technical Articles." Accessed: May 25, 2025. [Online]. Available:

https://eepower.com/technical-articles/understanding-the-electrical-properties-of-conductors-insulators-and-semiconductors/

[31] "1. Schematic diagrams of band structures and recombinations in (a)... | Download Scientific Diagram." Accessed: May 25, 2025. [Online]. Available: https://www.researchgate.net/figure/Schematic-diagrams-of-band-structures-and-recombinations-in-a-direct-bandgap_fig1_303523076

[32] N. Rahimi, R. A. Pax, and E. MacA. Gray, "Review of functional titanium oxides. I: TiO2 and its modifications," *Progress in Solid State Chemistry*, vol. 44, no. 3, pp. 86–105, 2016, doi: https://doi.org/10.1016/j.progsolidstchem.2016.07.002.

[33] "TITANIUM DIOXIDE APPLICATIONS, SYNTHESIS AND TOXICITY PRAFULLA K. JHA EDITOR New York," 2013. [Online]. Available: http://www.novapublishers.com

[34] X. Chen and S. S. Mao, "Titanium dioxide nanomaterials: Synthesis, properties, modifications and applications," Jul. 2007. doi: 10.1021/cr0500535.

[35] A. H. Navidpour, S. Abbasi, D. Li, A. Mojiri, and J. L. Zhou, "Investigation of Advanced Oxidation Process in the Presence of TiO2 Semiconductor as Photocatalyst: Property, Principle, Kinetic Analysis, and Photocatalytic Activity," Feb. 01, 2023, *MDPI*. doi: 10.3390/catal13020232.

[36] M. R. Johan, M. S. M. Suan, N. L. Hawari, and H. A. Ching, "Annealing Effects on the Properties of Copper Oxide Thin Films Prepared by Chemical Deposition," *Int J Electrochem Sci*, vol. 6, no. 12, pp. 6094–6104, 2011, doi: https://doi.org/10.1016/S1452-3981(23)19665-9.

[37] K. Lyon, A. Zakhidov, and C. E. Piner, "COPPER IODIDE AND COPPER (I) OXIDE BASED HOLE TRANSPORT MATERIALS FOR METHYLAMMONIUM LEAD IODIDE PHOTOVOLTAIC DEVICE OPTIMIZATION Mark Wistey," 2019.

[38] M. Umar, "Deposition and Characterization of Wide Band Gap P-Type Metal Oxides for Photovoltaic Applications," University_of_Basel, 2022.

[39] A. M. El-Khawaga, A. Zidan, and A. I. A. A. El-Mageed, "Preparation methods of different nanomaterials for various potential applications: A review," *J Mol Struct*, vol. 1281, Jun. 2023, doi: 10.1016/j.molstruc.2023.135148.

[40] W. Han, H. Jiao, and D. Fox, "Scanning electron microscopy," in *Springer Tracts in Modern Physics*, vol. 272, Springer Verlag, 2018, pp. 35–68. doi: 10.1007/978-981-13-0454-5_2.

[41] "□ Schematic diagram of SEM 1 | Download Scientific Diagram." Accessed: May 25, 2025. [Online]. Available: https://www.researchgate.net/figure/Schematic-diagram-of-SEM-1_fig3_235672359

[42] Y. Waseda, E. Matsubara, and K. Shinoda, "Diffraction from Polycrystalline Samples and Determination of Crystal Structure," *X-Ray Diffraction Crystallography*, pp. 107–167, 2011, doi: 10.1007/978-3-642-16635-8_4.

[43] "X_Ray_Diffraction_Crystallography_Introduction_Ex".

[44] S. A. Bo, P. Y. Yee, and R. Y. Ttl, "FOURIER TRANSFORM FAD."

[45] Administrator, "CHAP 10."

[46] "Shimadzu XRD-6000 X-ray Diffractometer." Accessed: May 25, 2025. [Online]. Available: https://hitechtrader.com/shimadzu-xrd-6000-x-ray-diffractometer/

[47] D. Harvey, *Analytical Chemistry 2.0*. LibreTexts, 2010.

[48] "Luminous Color Measurement by UV-Visible Spectroscopy | JASCO." Accessed: May 25, 2025. [Online]. Available: https://jascoinc.com/applications/luminous-color-measurement/

[49] "Infrared Spectroscopy | GeeksforGeeks." Accessed: May 25, 2025. [Online]. Available: https://www.geeksforgeeks.org/infrared-spectroscopy/

الملخص

ثاني أكسيد التيتانيوم TiO_2 المطعم بمركبات CuO النانوية هي واحدة من أكثر المواد قدرة على توفير الطاقة الشمسية الفعالة من حيث التكلفة والموثوقة بالإضافة إلى تطوير بدائل تجارية في إنتاج الطاقة الشمسية وتخزين الطاقة مع زيادة كفاءتها في التطبيقات المرغوبة. يهدف هذا البحث إلى استقصاء تأثير الإضافة على الخصائص البصرية والهيكلية ل TiO_2 باستخدام طريقة Sol-gel بتركيزات مختلفة تتراوح بين 5٪ و 15٪. تم فحص التركيب البلوري والخصائص البصرية للعينات المركبة باستخدام حيود الأشعة السينية (XRD) والتحليل الطيفي للأشعة فوق البنفسجية المرئية (UV) على التوالي. أظهرت جميع العينات بنية بلورية Anatase مع زيادة ملحوظة في حجم البلورة حيث زادت تنسيق CuO من 100.9 نانومتر إلى 207.3 نانومتر. بالإضافة إلى ذلك ، أثرت هذه الزيادة في النسب المئوية على المعلمات البصرية من خلال تعزيز الكفاءة البصرية للعينات المحضرة مع تحول طفيف ملحوظ إلى المنطقة المرئية لتحسين كفاءتها لاستخدامها كتطبيقات تحفيزية ضوئية وموفرة للطاقة بطرق أكثر موثوقية وفعالية. أسفرت هذه الدراسة عن رؤى مهمة قد تساعد في تطوير التطبيقات الإلكترونية الضوئية في الصناعات عن طريق تقليل التكاليف. ويمكن أن تكون هذه النتائج مفيدة في تعزيز عمليات الإنتاج والاستفادة من خيارات أكثر قابلية للتطبيق وفعالية من حيث التكلفة للعمليات الصناعية.

المملكة العربية السعودية
وزارة التعليم العالي
جامعة القصيم
كلية العلوم
قسم الفيزياء

دراسة التركيب والخصائص البصرية لأكسيد التيتانيوم المطعم بالمعادن

رسالة مقدمة لاستكمال متطلبات الحصول على درجة الماجستير في فيزياء الجوامد

اعداد
دلال عائض المطيري
(431214724)

إشراف
الدكتورة: عائشة بنت محمد الهديب
استاذ مشارك في كلية العلوم (قسم الفيزياء)

1446هـ/2025م